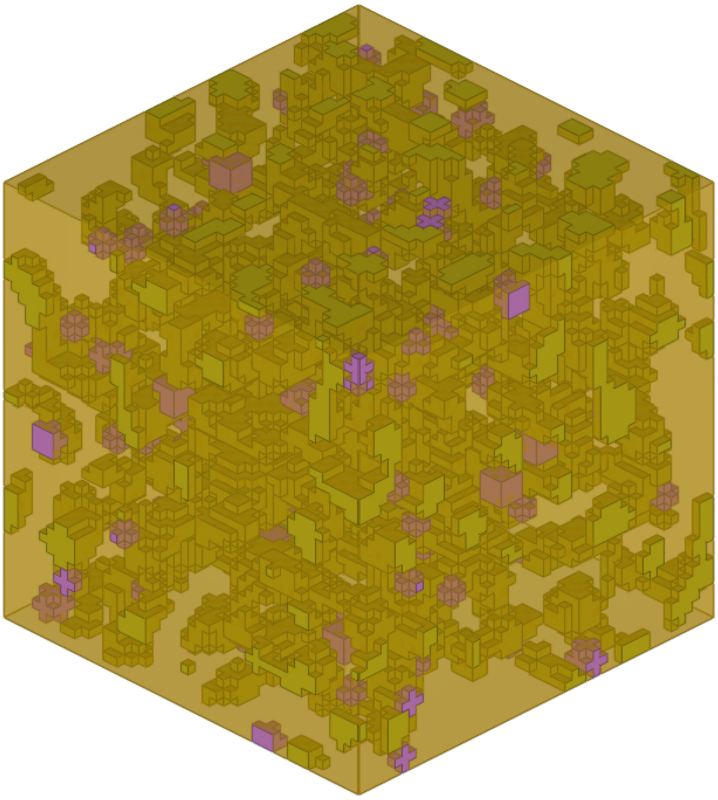

Micromechanical modeling of fracture in high-pressure die cast aluminum

Master's thesis in Mobility Engineering

WILLIAM ABEL
VALDEMAR KULLBERG

DEPARTMENT OF INDUSTRIAL AND MATERIALS SCIENCE
CHALMERS UNIVERSITY OF TECHNOLOGY
Gothenburg, Sweden 2026
www.chalmers.se

Master's thesis 2026 - IMSX30

Micromechanical modelling of fracture in high-pressure die cast aluminum

WILLIAM ABEL
VALDEMAR KULLBERG

Department of Industrial and Materials Science
Division of Material and Computational Mechanics
Chalmers University of Technology
Gothenburg, Sweden 2026

Micromechanical modeling of fracture in high-pressure die cast aluminum
WILLIAM ABEL
VALDEMAR KULLBERG

Supervisor: Robin Larsson, Volvo Cars Corporation.
Supervisor: Johann Körbelin, Volvo Cars Corporation.
Examiner: Prof. Magnus Ekh, Department of Industrial and Materials Science.

Master's Thesis 2026
Department of Industrial and Materials Science
Division of Material and Computational Mechanics
Chalmers University of Technology
SE-412 96 Gothenburg
Telephone +46 31 772 1000

Cover: Generated three-phase microstructure visualized in ANSA pre.

Typeset in LaTeX
Printed by Chalmers Reproservice
Gothenburg, Sweden 2026

Micromechanical modeling of fracture in high-pressure die cast aluminum
WILLIAM ABEL
VALDEMAR KULLBERG
Department of Industrial and Materials Science
Chalmers University of Technology

Abstract

High-pressure die cast aluminum is being incorporated into the production of electric vehicles in order to increase vehicle efficiency and reduce manufacturing costs. The process is known as Mega Casting and can produce large scale components with complex geometry in one process, drastically reducing the amount of welds and joints. Due to the process, the aluminum components possess a complex microstructure with different phases and porosity, which makes the mechanical properties difficult to predict. Today, there is a lack of Finite Element (FE) and material models that can capture these microstructural defects on a component scale.

Throughout the project, a method for generation of three-phase microstructure models based on Computer Tomography (CT) scanning and Scanning Electron Microscope (SEM) images is developed. Numerical studies on mesh design, time integration and boundary conditions are performed with the intention to optimize computational costs while maintaining accuracy. Furthermore, the variation in mechanical properties depending on morphology is studied by simulating a range of different microstructures subjected to different load cases.

The results show that it is possible to generate three-phase microstructures that represent the eutectic silicon region in HPDC-aluminum components. The choices of the numerical model and modeling have impact on computational efficiency and accuracy. Furthermore, it is possible to vary the internal morphology in the model in order to obtain mechanical response data for a wide range of microstructures.

Keywords: multiscale modeling, microstructure, HPDC aluminum, homogenization, finite element analysis, porosity, silicon particles, computational mechanics

Acknowledgements

We would like to express our gratitude to everyone who contributed to the completion of this master thesis. We would like to thank our supervisors Robin Larsson and Johann Körbelin for introducing the project to us, as well as guiding and supporting us along the project. We would also like to thank our examiner, Prof. Magnus Ekh, for supporting along the way and expanding our knowledge on topics regarding the project.

Microscopic images was taken at Chalmers Material lab, a special thanks to Margarita Mitsi for her consultation and providing these images based on our requests. Software from BETA CAE Systems have been used in this project, and we would like to thank Peter Appelgren for support regarding the software. We would also like to thank Mats Landervik for valuable support regarding LS-DYNA, and providing us with experimental versions of the software.

Volvo Cars has provided us with workspace, computers, software licenses and all necessary resources needed. We would like to thank them for making this possible. We would also like to thank the material team at Volvo Cars Safety Centre for high quality support and input regarding the content, and providing an inspiring working environment, including weekly fika.

William Abel & Valdemar Kullberg, Gothenburg, June 2026

List of Acronyms

Below is the list of acronyms that have been used throughout this thesis listed in alphabetical order:

2D	Two Dimensional
3D	Three Dimensional
CT	Computed Tomography
EV	Electric Vehicle
FE	Finite Element
FEA	Finite Element Analysis
FFT	Fast Fourier Transform
GRF	Gaussian Random Field
HPDC	High Pressure Die Casting
LDBC	Linear Displacement Boundary Conditions
OEM	Original Equipment Manufacturer
PBC	Periodic Boundary Conditions
RVE	Representative Volume Element
SEM	Scanning Electron Microscopy
SVE	Statistical Volume Element

Contents

List of Figures

List of Tables

1

Introduction

1.1 Background

The current trend in the automotive industry is moving towards E-mobility, with the aim to minimize carbon emissions and convert to a more sustainable future for travel. To achieve this goal, Original Equipment Manufacturers (OEMs) are designing vehicles for maximum efficiency such as minimizing aerodynamic drag, optimizing the powertrain or minimize weight [1]. For weight reduction, automotive manufacturers like Volvo Cars are implementing new methods. High-Pressure Die Cast (HPDC) is a manufacturing process that is being used more frequently in the automotive industry for aluminum-based alloys. The method is cost effective and efficient in large scale production as it is able to produce large complex components in one cycle with high accuracy [2]. The process greatly reduces the number of welds and joints in the components, which increases the energy efficiency and range of electric vehicles (EV). For large scale components this method is known as *Megacasting* in the automotive industry [3], [4].

The process of megacasting starts with molten aluminum being injected into a die cavity with high velocity. The cavity possesses the negative volume of the desired component. High pressure is applied to the aluminum as it enters the cavity, ranging from $40-160\ MPa$. The filling process is very fast, between $10-150\ ms$ depending on the size of the component. The metal is then cooled in the die until it solidifies. The two die halves are then separated, and the casted component is ejected out of the die by rods [5]. One drawback of HPDC aluminum is that it possesses a complex microstructure with variation of defects such as pores, silicon particles and intermetallics. Figure 1.1 visualizes the difference between analyzing the material on microscale in comparison to component level. The local variation of defects makes it difficult to predict the mechanical properties of the material. This is problematic since the local microscopic properties influence the macroscopic performance of the whole part [6].

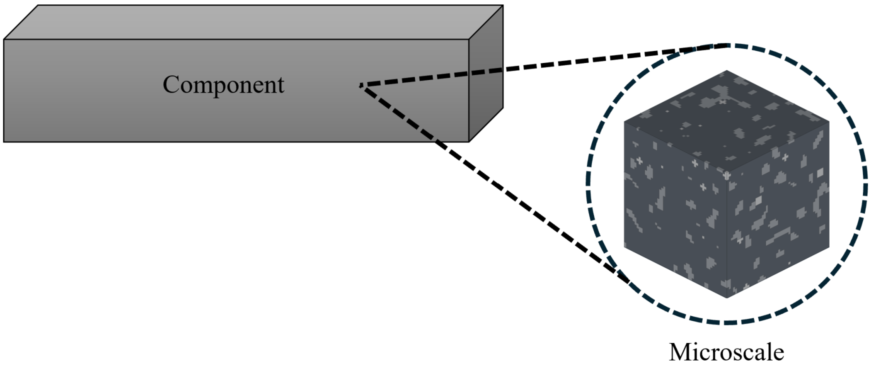

Figure 1.1: Visualization of complex microstructure in an HPDC aluminum component.

Material behavior is impacted by factors that span over different scales. Crack propagation in aluminum alloys are governed by features on the microscale, but also loading condition on macroscale. Multiscale modeling is a method for linking these phenomena between scales. One way of doing this is by conducting simulations on different scales in order to calibrate a homogeneous material model that can be used for components [7]. A description of the method is presented in Figure 1.2. There are some previous projects that have investigated multiscale modeling for materials with a varying stochastic morphology. In 2024, a bachelor thesis at Chalmers University of Technology in cooperation with Volvo Cars investigated statistical variation of natural fiber composites. This was done by extracting volume elements on microscale, and analyzing how the volume elements correlated with the large model mechanically. The results concluded that volume elements from a larger model could be used to simulate many different microstructures in order to obtain statistical data of mechanical behavior [8]. The similarity between natural fiber composites and HPDC aluminum is the stochastic morphology.

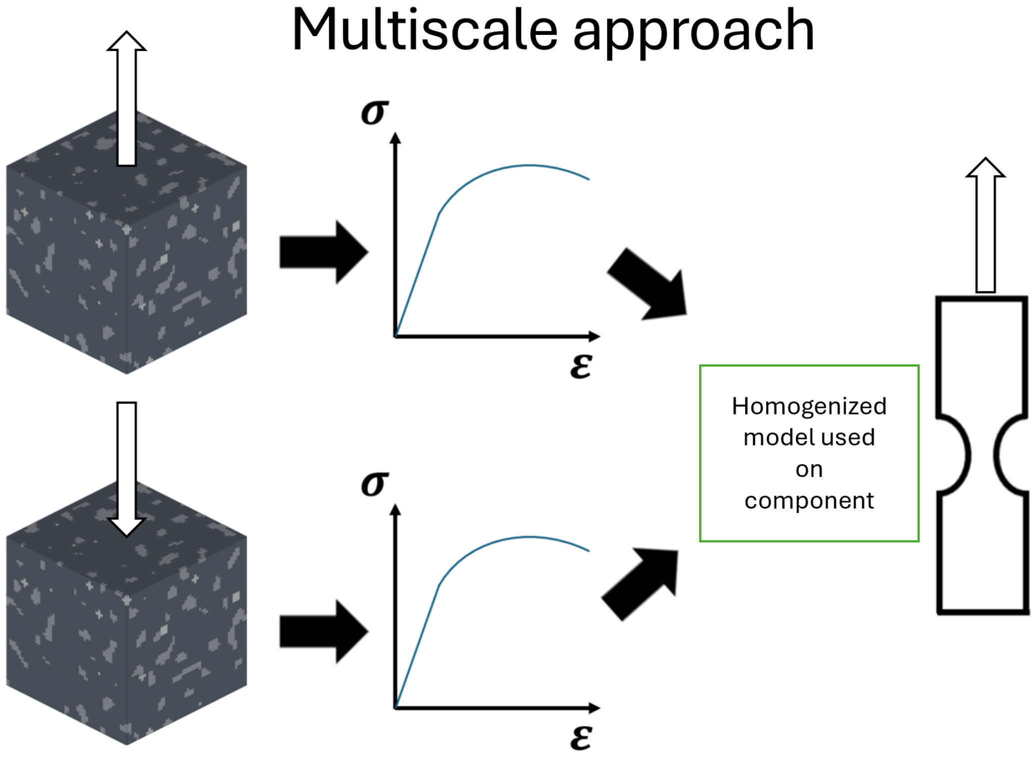

Figure 1.2: The process of multiscale modeling. Extracting data of micromechanical properties and applying it on component level.

1.2 Objective

The objective of this thesis is to develop a method that creates representative microstructures in order to analyze how variations in defects within the microstructure of HPDC aluminum influence its mechanical behavior, while taking into account the effects of different FE mesh strategies, mesh resolutions, boundary conditions, and time integration techniques with respect to accuracy and computational cost.

1.3 Limitations

The project has set limitations to ensure it is possible to conduct with the given time frame and resources.

- The modeling and analysis on microscale only features the eutectic silicon region.
- Experimental testing will not be conducted.
- Only Periodic Boundary Conditions (PBC) and Linear Displacement Boundary Conditions (LDBC) are used for simulations.

2

Microstructure of HPDC aluminum

This chapter describes,

- what is known about the microstructure from experimental characterization
- then present the procedure to define numerical models of typical microstructures with common constituents and defects.

2.1 Overview

Aluminum-silicon (Al-Si) alloys are commonly used in casting applications of complex geometries due to their superior castability as opposed to other alloys. The silicon serves as the main alloying substance and provides high fluidity, low shrinkage and reduced thermal expansion. The volume fraction of silicon in Al-Si compositions is usually $5 - 20$ wt.% for casting applications [9]. The addition of silicon in aluminum alloys can also increase strength by formation of hard silicon phases. However, this comes with a cost of decreased ductility. The silicon can also interact with aluminum and iron to form intermetallic phases, which also decrease the ductility of the casted component [10]. The intermetallic phase will however not be modeled in this project. Figure 2.1 shows an image of the microstructural phases in an Al-Si test specimen through a Scanning Electron Microscope (SEM), conducted at Chalmers material lab.

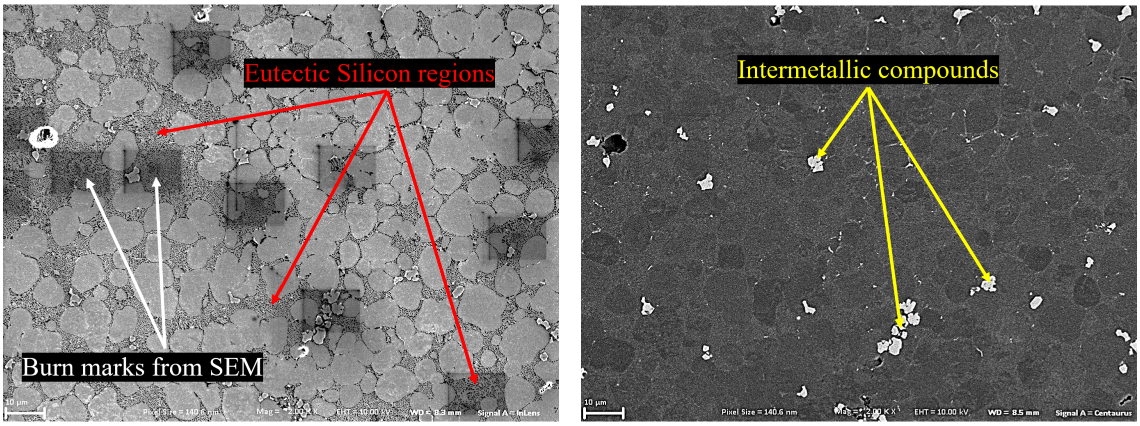

(a) Low contrast image.

(b) High contrast image.

Figure 2.1: SEM image of microstructure in a) Low contrast, and b) High contrast, to visualize phase distribution in an Al-Si alloy. Image courtesy of Margarita Mitsi.

One of the common defects in HPDC aluminum components is porosity, which means that there are internal voids of air forming during the manufacturing process. The high speed filling process gives rise to turbulent flow. This leads to gas entrapment in the material, known as gas porosity. The aluminum also shrinks during the solidification process, which means that there will be less volume occupied by the aluminum. This leads to air voids forming, known as shrinkage porosity. The porosity distribution can be predicted on component level, it increases farther away from the inlet of the cavity. However, it is difficult to predict the porosity on a microscale, which leads to difficulties in predicting the mechanical properties locally [2].

2.2 Eutectic Silicon regions

During solidification of HPDC Al-Si alloys, eutectic silicon regions form in the microstructure at 577 $°C$. In these regions, the liquid solution transforms into two solid phases: α-aluminum and silicon particles. Silicon content in the eutectic regions is around 12 wt.%. The solidification rate of the solution determines the grain size and distribution of silicon particles. Rapid solidification results in a fine eutectic structure with small grain sizes, and slow solidification results in a coarse microstructure with large silicon particles in a matrix of α-aluminum. Coarse silicon particles lowers the strength and ductility of the eutectic alloy. The variation in shape of these silicon particles also affect the mechanical properties [11]. Figure 2.2 shows a SEM image of an eutectic silicon region in an Al-Si alloy.

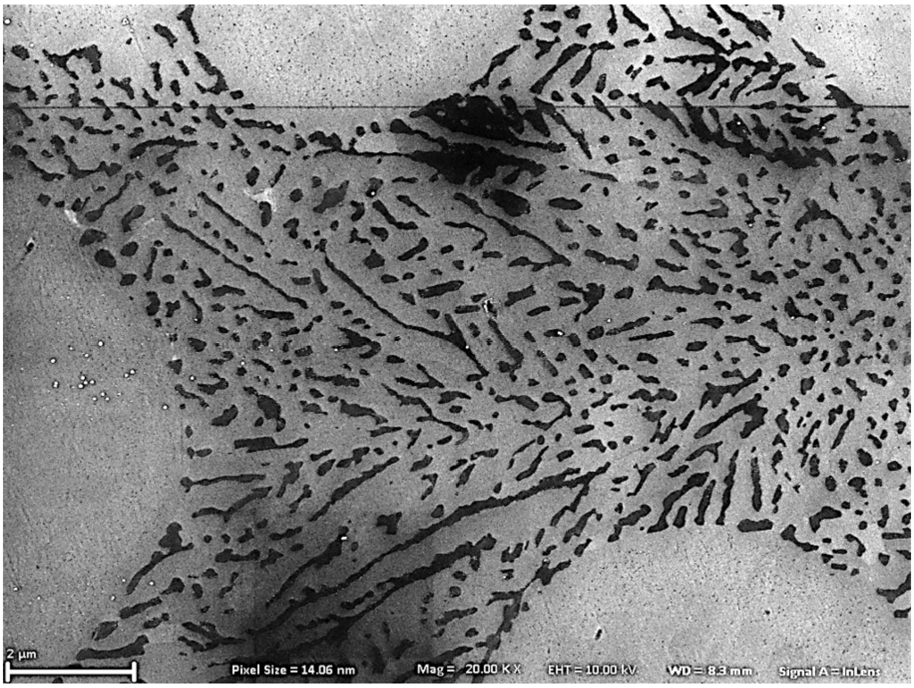

Figure 2.2: SEM image of eutectic region in an Al-Si alloy. Light gray area is α-aluminum and the dark gray area is the silicon particles. Image courtesy of Margarita Mitsi

2.3 From 2D image to 3D voxel representation

In order to obtain statistical variation of the micromechanical properties of HPDC aluminum, a large variation of microstructures must be simulated. Microstructure data can be obtained through X-ray computed tomography (CT-scan), which gives a high resolution 3-D image with segmented phases (solid aluminum and porosity). The segmentation image can then be converted to an FE model. Both the segmentation process and conversion to an FE model can be done with the software RETOMO. However, this process is costly and time consuming as each model needs CT-scanning and segmentation of the different phases. Furthermore, it is not possible to control the microstructure, and the amount of porosity and its distribution cannot be determined before scanning. This method is therefore less appropriate when a large number of unique microstructures should be simulated to obtain the spread of the effective properties in the material.

Another way is to use software that automatically generates models of the microstructures. In the software, parameters such as volume fraction, grain size and grain count can be adjusted accordingly based on images from SEM analysis, as the one in Figure 2.1. It is also much more efficient since numerous unique microstructures can be generated in a short time without the need of CT-scanning. In this project, the software GRFsaw[12] is used as a generator for numerical microstructure models. GRFsaw is an open source lightweight stochastic microstructure generator developed by Lars Blatny et al. [13] at the Institute for Geotechnical Engineering in Zürich, Switzerland [14]. Microstructures can then be generated based on information from both CT-scans and SEM images. The algorithm in GRF-saw is based on that Gaussian Random Fields (GRFs) are constructed by adding many cosine waves together, and thresholding the values in order to build the different phases. The GRF is defined as:

$$GRF(\mathbf{r}) = \frac{1}{\sqrt{N}} \sum_{n=1}^{N} cos(\mathbf{q}_n \cdot \mathbf{r} + \varphi_n) \tag{2.1}$$

where $\mathbf{q}_n$ are the wave vectors, N is the number of waves and φ_n are random variables ranging from 0 to 2π. A binary microstructure is constructed by thresholding $GRF(\mathbf{r})$ with the desired solid volume fraction:

$$\phi = \frac{V_{solid}}{V_{total}} \tag{2.2}$$

$$c(\phi) = \mathrm{erf}^{-1}(1 - 2\phi) \tag{2.3}$$

where erf is Gauss's error function:

$$\mathrm{erf}(x) = \frac{2}{\sqrt{\pi}} \int_0^x e^{-t^2} dt \tag{2.4}$$

The phases in the microstructure are then determined by the threshold:

$$Z(\mathbf{r}) = \begin{cases} 1, & \textbf{if } GRF(\mathbf{r}) > c(\phi) \\ 0, & \textbf{if } GRF(\mathbf{r}) \leq c(\phi) \end{cases} \tag{2.5}$$

where $Z(\mathbf{r}) = 1$ is a solid phase and $Z(\mathbf{r}) = 0$ is a void phase.

A simpler explanation of the process is to imagine rocks thrown into a pond, shown in Figure 2.3a. The specified seed determine the location where the rocks are thrown, i.e the initial locations where the waves are generated. As the waves collide with each other, the amplitude either increase or decrease. The phases are then determined by threshold of the wave amplitude, as shown in Figure 2.3b. The outcome from this case is a 2D two-phase microstructure, an example is shown in Figure 2.4. For 3D microstructure the method is the same, but the waves are traveling in 3D space like shock waves.

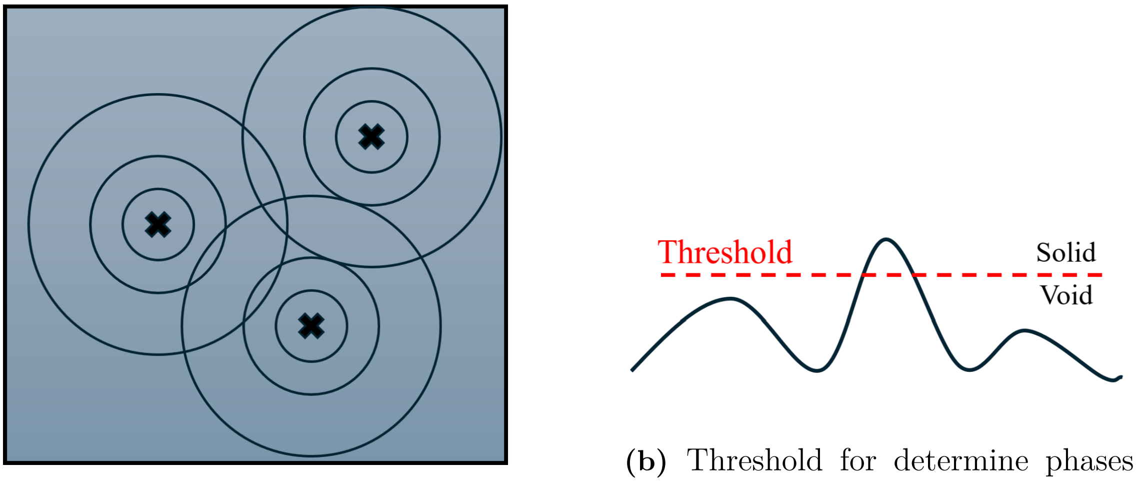

(a) Seed points and waves.

(b) Threshold for determine phases based on amplitude.

Figure 2.3: Visualization of microstructure generation with GRFsaw.

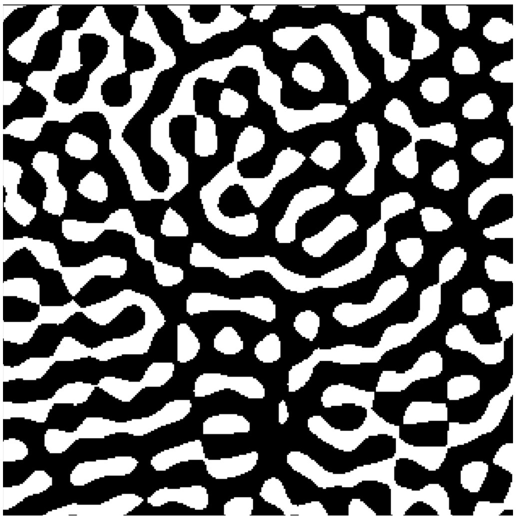

Figure 2.4: Example of a 2D microstructure generated with GRFsaw.

The wave vectors are defined as $\mathbf{q}_n = 2\pi/\lambda_n \hat{\mathbf{q}}_n$, where their magnitude $2\pi/\lambda_n$ and direction $\hat{\mathbf{q}}_n$ is sampled in order to alter the microstructural elements size and distribution. If $\langle\lambda\rangle$ is the average sampled wavelength and L is the length of the microstructure, the average number of microstructural elements per length can be expressed as $\langle m\rangle = L/\langle\lambda\rangle$. The target particle size can therefore be adjusted with probability distributions of mean $\langle m\rangle$ and standard deviation Δm. Furthermore, the desired mesh points in each direction are defined as a vector $[x, y, z]$ [13].

One limitation with GRFsaw is that the Gaussian random fields can only be used to generate two-phase microstructures. If three phases or more is of interest they need to be added outside GRF-saw. It is therefore easier if the third phase has simple shapes like spheres or cubes. The phase that has larger volume fraction and most irregular shape should be generated as the primary phase.

The output from GRFsaw is a list with coordinates for every solid voxel. The porous phase is not modeled and there are no coordinates defined for those voxels. In order to convert the output into an LS-DYNA mesh file, scripting in Python is used to format and define node coordinates and element nodes. The empty space that occupies the porous phase is filled with hexahedral elements with a different part ID. The third phase is added by creating spherical shapes that are distributed randomly inside the aluminum volume, and is prevented from overlapping with the silicon particles. The desired voxel radius and size deviation of these shapes is defined. In order to achieve phases with different shapes and geometry, the seed for each attempt is changed, resulting in volume elements with different microstructures but constant volume fractions. Based on SEM images of the eutectic silicon region, the parameters defined in Table 2.1 is used to as input for microstructure generations. This is further explained in Section 3.3. Figure 2.5 shows an example of a generated three-phase voxel mesh with the chosen input parameters.

Table 2.1: Input parameters for generating microstructures in GRFsaw.

Parameter	**Value**	**Description**
ϕ_{Al}	0.87	Aluminum volume fraction.
ϕ_{Sl}	0.12	Silicon volume fraction.
$\phi_{Porosity}$	0.01	Porosity volume fraction.
m_{mean}	7	Mean particle size (silicon).
m_{std}	1.2	Standard deviation of particle size (silicon).
r_{pore}	2	Radius of pores as number of voxels.
r_{std}	0.5	Standard deviation of pore radius.

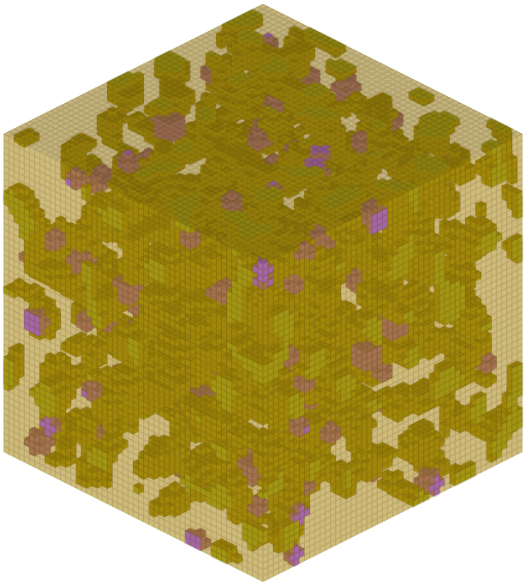

Figure 2.5: LS-DYNA mesh of generated microstructure.
Aluminum: Transparent, Silicon: Yellow, Pores: Pink

3

Eutectic simulation model

This chapter presents the material modeling, homogenization methodology, how the FE mesh compares to the SEM images and how the boundary condition and load is applied.

3.1 Material modeling

In order to capture a realistic mechanical response from FE-analysis of the microstructure simulations, the different phases have to be modeled correctly with their own unique material properties. In LS-DYNA, this is achieved by assigning specific material cards to the different phases. There are many different material cards in LS-DYNA which can be selected from depending on how the physical material behaves.

3.1.1 Aluminum phase

The aluminum phase is modeled using the material card *MAT_PIECEWISE_LINEAR_PLASTICITY, also referred to as *MAT_024 in LS-DYNA. This material model describes elasto-plastic behavior, where the elastic region is defined by Young´s modulus and Poisson's ratio. The plastic region is defined by an analytical hardening law, in this case the Hockett-Sherby equation.

$$\sigma = A - Be^{C\varepsilon_p^H} \tag{3.1}$$

Hockett-Sherby is a continuous function describing the evolution of flow stress, σ, with plastic strain, ε_p. During the numerical solution, LS-DYNA evaluates this function at discrete points and constructs a piecewise linear approximation of the curve. The number of sampling points is controlled by the *CONTROL_SOLUTION card.

The first stress value obtained from the discretized curve, when $\varepsilon_p = 0$, corresponds to the yield limit and defines the onset of plastic deformation [15].

3.1.2 Damage model

To accurately model fracture in a FE-model, a damage model can be used to introduce material degradation. An example of such a damage model is GISSMO

(*Generalized Incremental Stress-State dependent damage MOdel*) [16]. It features incremental damage accumulation during the loading history and includes softening and failure. Instead of just defining failure strain for the material, damage is accumulated over time depending on stress state and plastic strain. The plastic failure strain for each element is determined by the stress state, which is defined with a triaxiality curve. This damage model is often used for ductile failure of metals and uses tabulated input data from physical testing. Equation 3.2 shows how GISSMO calculates incremental damage accumulation [15].

$$\Delta D = \frac{D_{\text{exp}} \cdot D^{\left(1-\frac{1}{D_{\text{exp}}}\right)}}{\varepsilon_f} \Delta \varepsilon_p \tag{3.2}$$

where D is the Damage value ($0 \leq D \leq 1$). Elements are eroded if $D \geq 1$. The equivalent plastic strain to failure ε_f is defined by tabulated data of stress triaxiality and plastic failure strain, $\Delta\varepsilon_p$. An example of a stress triaxiality curve is presented in Figure 3.1.

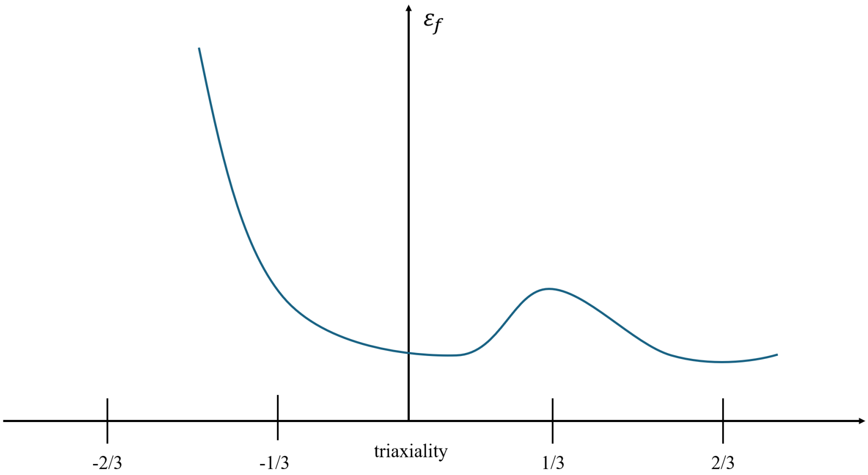

Figure 3.1: Example of relation between plastic failure strain and stress triaxiality.

The stress triaxiality factor η is defined as the ratio of hydrostatic stress, σ_H, and von Mises equivalent stress, σ_{eq}.

$$\eta = \frac{\sigma_H}{\sigma_{eq}} = \frac{\frac{1}{3}\left(\sigma_{11} + \sigma_{22} + \sigma_{33}\right)}{\sqrt{\frac{(\sigma_{11}-\sigma_{22})^2+(\sigma_{22}-\sigma_{33})^2+(\sigma_{33}-\sigma_{11})^2+6\left(\sigma_{12}^2+\sigma_{23}^2+\sigma_{31}^2\right)}{2}}} \tag{3.3}$$

Stress triaxiality describes the overall stress condition and a high (positive) value indicates that the stress mode promotes crack opening. Different triaxiality factors are achieved by conducting different load cases in physical testing [17].

Table 3.1: Stress triaxiality factors for common load cases [18].

Load case	Triaxiality factor η
Biaxial compression	$-2/3$
Uniaxial compression	$-1/3$
Pure shear	0
Uniaxial tension	$1/3$
Laterally confined tension	$1/\sqrt{3}$
Biaxial tension	$2/3$

Note that the exact values of triaxiality in the table are only obtained if the microstructure and stress field are homogeneous. If pores and other particles is added, as in this case, these values can vary.

3.1.3 Modeling of pores

The pores in the material were chosen to be modeled with soft elasticity instead of not excluding (eroding) the elements. The reason is to increase the numerical stability. Therefore, *MAT_ELASTIC, also labeled *MAT_001 in LS-DYNA, is used. For this card, only the density, Young's modulus and Poisson's ratio needs to be defined. The density and Poisson's ratio was kept the same as for aluminum but Young's modulus was decreased from 75GPa to 0.01GPa.

3.1.4 Modeling of Silicon

The silicon is modeled with *MAT_MODIFIED_PIECEWISE_LINEAR_PLASTICITY, also labeled *MAT_123, in LS-DYNA. This card is similar to the one used for aluminum, *MAT_024, but offers different implemented failure criteria [15] than GISSMO. This was chosen since there was no GISSMO parameters defined for silicon during this project. Instead maximum principal strain criteria is used without any incremental softening (uncoupled damage model). Failure is reached when the maximum principal strain reaches $EPSMAJ$. In this model, $EPSMAJ = 0.04$.

The elastic and plastic region for the silicon was scaled by doubling both the Young's modulus and the stress components in the Hockett-Sherby law as compared to the model for the aluminum phase.

3.2 Homogenization

Based on Figure 2.3a, the eutectic region has a total length of $10\mu m$ and when this mesh is generated it consists of 125 000 elements. The large amount of elements is needed in order to capture the complex morphology of the microstructure with α-aluminum, silicon particles and voids. Such detailed model is however not feasible to use in FE simulations of components due to the high computational cost.

Therefore, representative FE-models of the microstructure can be used to predict effective (homogenized) properties. These properties can later be used to define the behavior of components, [19].

The homogenized stress, $\bar{\sigma}$, is computed as the volume-weighted average of the stress, σ_e, over all elements in the model. Similarly, the homogenized strain, $\bar{\varepsilon}$, is obtained as the volume-weighted average of the elements strain, ε_e.

$$\bar{\sigma} = \frac{1}{V} \sum_{e=1}^{n_{elem}} V_e \sigma_e \tag{3.4}$$

$$\bar{\varepsilon} = \frac{1}{V} \sum_{e=1}^{n_{elem}} V_e \varepsilon_e \tag{3.5}$$

Since we use a structured hexahedral mesh, where each element has the same volume length, these expressions can be simplified. In this case, the homogenized response is obtained by summing the stress and strain of all elements and dividing by the total number of elements, N.

$$\bar{\sigma} = \frac{1}{N} \sum_{e=1}^{n_{elem}} \sigma_e \tag{3.6}$$

$$\bar{\varepsilon} = \frac{1}{N} \sum_{e=1}^{n_{elem}} \varepsilon_e \tag{3.7}$$

3.3 FE mesh based on SEM images

As mentioned in Section 2.3, the output from the GRFsaw script is an LS-DYNA mesh file containing nodes, elements and parts. In order to evaluate whether this mesh is representative, a visual comparison is performed between the silicon particles observed in the SEM images and those in the generated mesh, this is presented below.

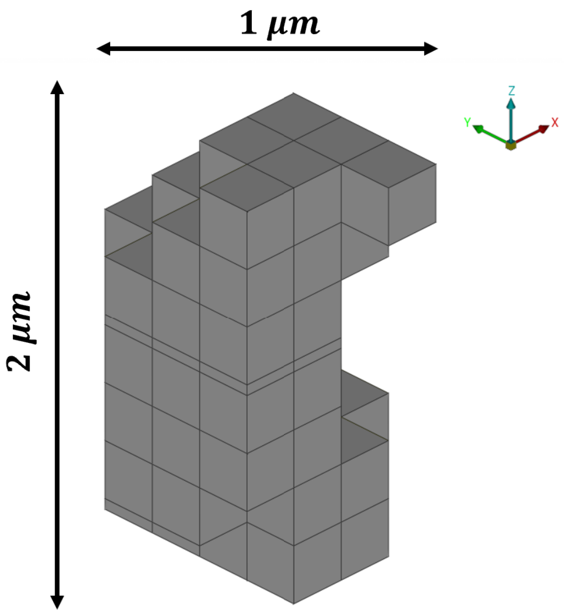

Figure 3.2: Example of silicon particle generated with GRFsaw.

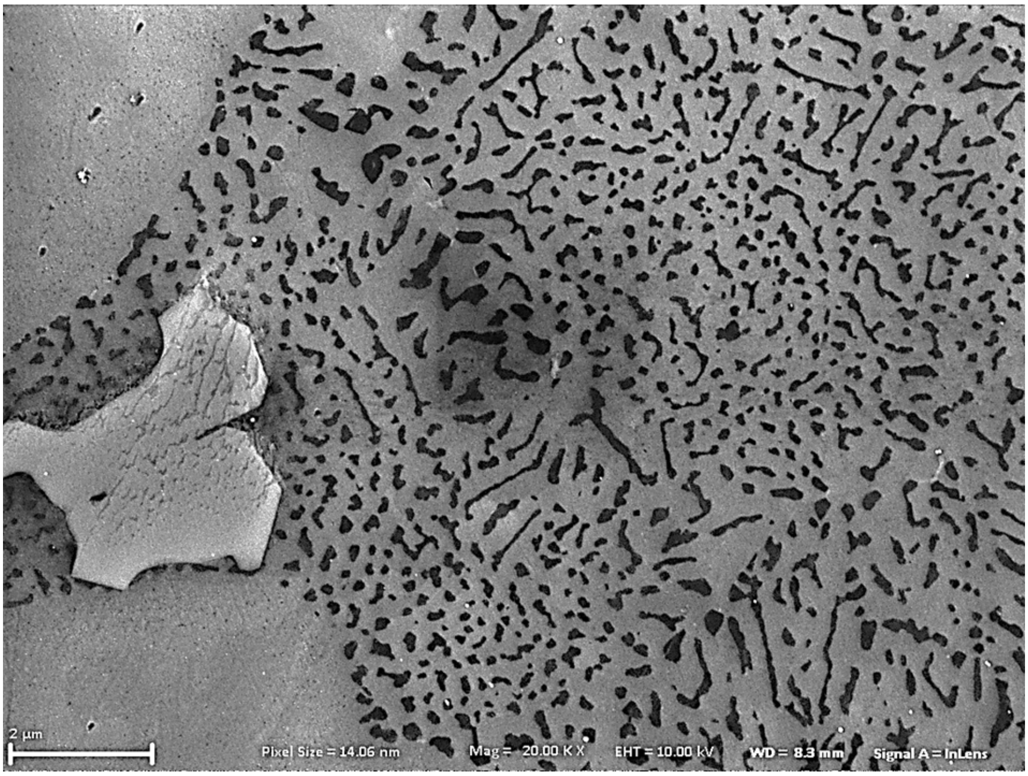

Figure 3.3: SEM image of eutectic silicon region.

Figure 3.2 shows one average size meshed silicon particle generated with GRFsaw. This particle is compared to the real silicon particles shown in Figure 3.3. In this SEM image, the lightest gray area is an intermetallic phase, the slightly darker gray is aluminum and the black spots are silicon particles.

The general shape of the particles in the mesh and the SEM image is matching. The length of the particles in generated mesh is allowed to be $1.5\mu m - 3.5\mu m$.

Based on both the mesh study, done later in Section 4.2, and the comparison between the mesh and the SEM image, the microstructure of the model is considered to be representative.

3.4 Boundary conditions and load cases

To achieve a homogenized representation of the fracture behavior, simulations must be performed for several distinct load cases. In LS-DYNA, there is a dedicated option for micromechanical simulations on volume elements with the keyword *RVE_ANALYSIS_FEM. By using this keyword we can automatically apply appropriate boundary conditions and provide homogenized results [20]. This section presents and compares these boundary conditions, and also analyze the mechanical response of different load cases.

3.4.1 Periodic boundary conditions

Periodic Boundary Conditions (PBC) can be used to simulate a volume element by applying the same displacement on opposite boundaries. By doing so, the volume element acts as if it is part of a large continuous volume when simulated.

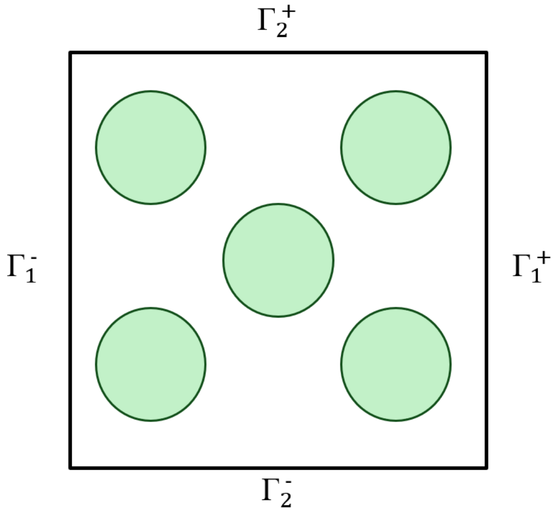

Figure 3.4: Periodic boundary conditions demonstrated on a two-phase volume element in 2D. The opposite boundaries are denoted Γ^+ and Γ^-. Inspired by [20].

Let $\mathbf{X_a^+}$ and $\mathbf{X_a^-}$ be material points located on opposite boundaries Γ_a^+ and Γ_a^- (see Figure 3.4). The periodic boundary conditions are defined as:

$$\mathbf{w_a^+} - \mathbf{w_a^-} = \tilde{\mathbf{H}}(\mathbf{X_a^+} - \mathbf{X_a^-}) \tag{3.8}$$

where **a** represents the dimensions x, y or z for 3D cases. The displacement of the material points are denoted **w** and are defined by the macroscopic displacement gradient $\tilde{\mathbf{H}}$. The boundary conditions are prescribed by components of the macroscopic displacement gradient showed in Equation 3.9 [20].

$$\tilde{\mathbf{H}} = \begin{bmatrix} H_{11} & H_{12} & H_{13} \\ H_{21} & H_{22} & H_{23} \\ H_{31} & H_{32} & H_{33} \end{bmatrix} = \begin{bmatrix} H_{xx} & H_{xy} & H_{xz} \\ H_{yx} & H_{yy} & H_{yz} \\ H_{zx} & H_{zy} & H_{zz} \end{bmatrix} \tag{3.9}$$

3.4.2 Linear displacement boundary conditions

Another type of boundary conditions suitable for volume elements are Linear Displacement Boundary Conditions (LDBC). The boundary conditions are imposed as following:

$$\mathbf{w}_a = \tilde{\mathbf{H}}\mathbf{X}_a \tag{3.10}$$

The term $\mathbf{X}_a$ denotes any material points at the opposite external boundaries Γ_a^+ and Γ_a^-. This means that the displacement of the boundaries are governed by Equation 3.10. Unlike PBC, this does not require any node pairing which facilitate manual pre-processing of FE-simulations. It is also possible to simulate non uniform meshes with this type, which is not possible with PBC since matching opposite boundaries are required for node pairing. However, volume elements usually appear stiffer when LDBC is applied in comparison to PBC [20]. The application of both PBC and LDBC are set up automatically in LS-DYNA, and there is no need for manual pre-processing. Hence, the most preferable option in this case is PBC.

3.4.3 Load cases

In order get a complete (multiaxial) homogenized response of the model, a set of different load cases are simulated. This is done by defining the components of the macroscopic displacement gradient $\tilde{\mathbf{H}}$, given in Equation 3.9. In LS-DYNA, this is adjusted with the *RVE_ANALYSIS_FEM keyword. The components of $\tilde{\mathbf{H}}$ include H_{11}, H_{22}, H_{33}, H_{12}, H_{13} and H_{23}. The components represent the directions x, y and z as showed in Equation 3.9. The primary load cases used in this project is tensile, laterally confined tensile, compression, biaxial tensile and pure shear. Figure 3.5 demonstrate these load cases.

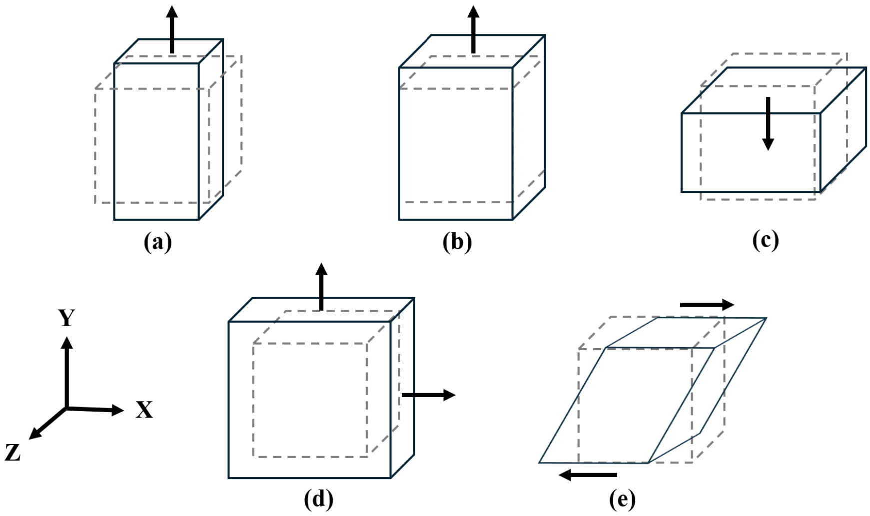

Figure 3.5: Visualization of load cases, where the dashed lines represent the initial shape of the specimen. a) Tensile, b) Laterally confined tensile, c) Compression, d) Biaxial tensile and e) Pure shear.

When simulating these load cases, the goal is to represent physical tests with the corresponding virtual load cases. The input values for the final macroscopic displacement gradient components are presented in Table 3.2. The components are linearly increased with time until the final values are reached (or failure has occurred). Note that for the unconstrained boundaries, no input values are given. If a value of zero is defined for a component, the prescribed and induced macroscopic displacement in this direction is zero. This is noted for lateral confined tension, where $H_{11} = 0$ in order to prevent the model from deforming in the x-direction. There are many different combinations of inputs that can create unique load cases. Table 3.2 describes how the load cases are defined with the components of the macroscopic displacement gradient. $H = 0.1$ corresponds to 10% macroscopic strain.

Table 3.2: Defined macroscopic displacement gradient components in for every load case.

Load case	H_{xx}	H_{yy}	H_{zz}	H_{xy}	H_{xz}	H_{yz}
Tensile	-	0.1	-	-	-	-
Laterally Confined Tensile	0	0.1	-	-	-	-
Compression	-	-0.1	-	-	-	-
Biaxial Tensile	0.1	0.1	-	-	-	-
Pure shear	-	-	-	0.1	-	-

The stress–strain response for the load cases listed in Table 3.2 is shown in Figure 3.6, with the exception of compression. For pure compression, failure is not observed in the simulations, making the corresponding results unreliable and therefore excluded.

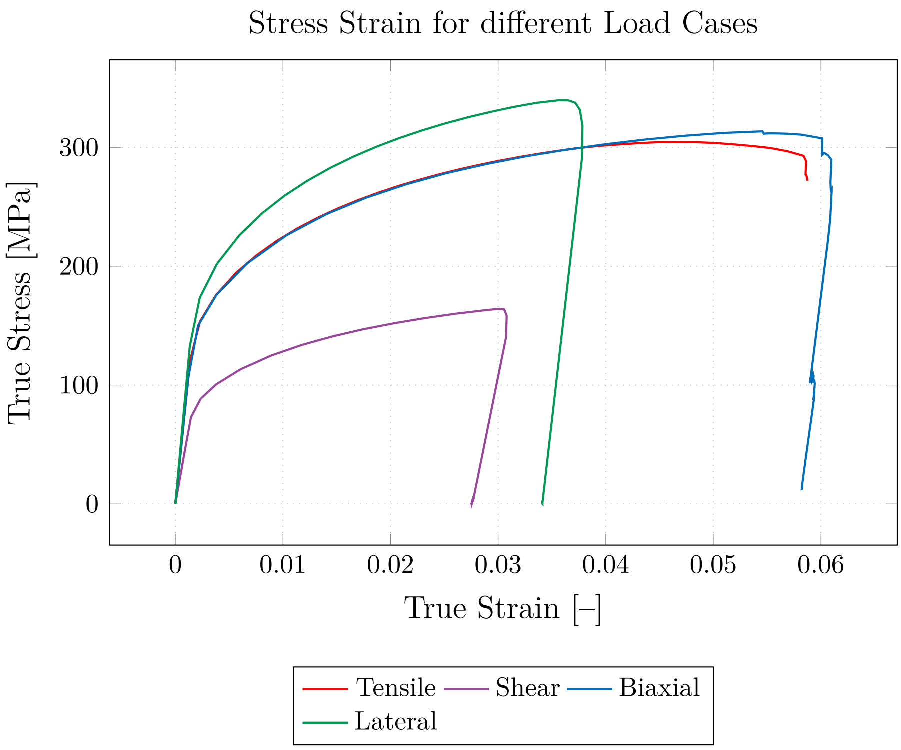

Figure 3.6: Stress-strain for the standard load cases.

In this stress–strain curve, the lateral and tensile load cases are represented by σ_{yy}, the biaxial load case by the average stress $\frac{\sigma_{yy}+\sigma_{xx}}{2}$, and the shear load case by τ_{xy}.

4

Numerical studies

This Chapter presents the numerical studies that are carried out in the project. This includes studies of boundary conditions, mesh size, mesh element, volume elements and time integration for the simulations.

4.1 Numerical comparison of periodic and linear displacement boundary condition

To establish if PBC or LDBC should be used, a comparison of the stress-strain response from a tensile test of an eutectic region is shown in Figure 4.1.

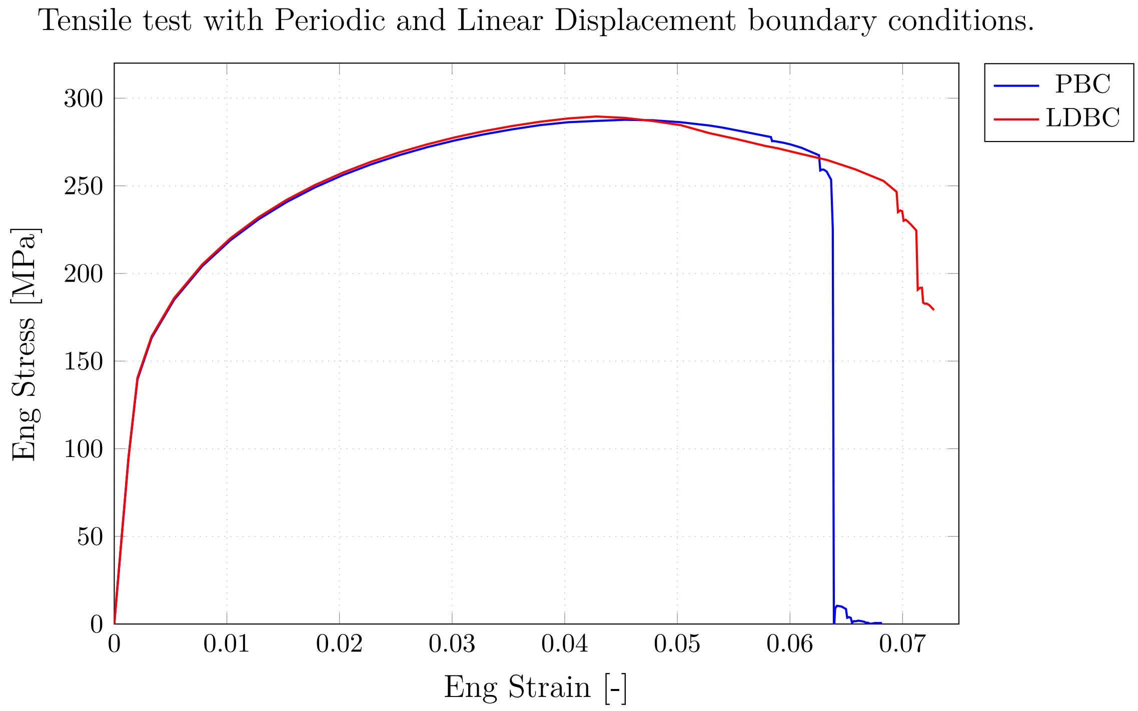

Figure 4.1: PBC vs Linear

The sudden drop in stress for both PBC and LDBC is where the volume element experiences fracture. Since the simulation model is completely fractured at this point, the stress-strain data after this event is not of interest. Consistent with the theoretical expectations outlined in the LS-DYNA Keyword Manual [20], the simulation with LDBC results in a stiffer material response compared to PBC. The LDBC does not allow for fracture close to the boundaries of the volume element. Therefore, PBC is assumed to be a valid choice of boundary conditions.

4.2 Mesh convergence study of the eutectic simulation model

In order to optimize computational efficiency, a mesh convergence study by changing the element size is conducted. The benefit of performing simulations on a coarse mesh is that the computational cost decreases. However, the mesh size has to be sufficient in order to capture the complex geometry of the microstructure. The approach for this is to simulate with models generated with the same input settings (seed, particle size, volume fractions), but with different mesh element sizes. By comparing the mechanical response, conclusions can be drawn based on convergence. For this mesh convergence study, a constant side length of the volume element of $10\mu m$ is used. In Table 4.1 the element size, and the number of element, for the meshes used in the study are presented.

Table 4.1: Properties of evaluated meshes.

Mesh	**Element length (μm)**	**No. of elements**
Mesh 1	0.25	64 000
Mesh 2	0.20	125 000
Mesh 3	0.125	512 000

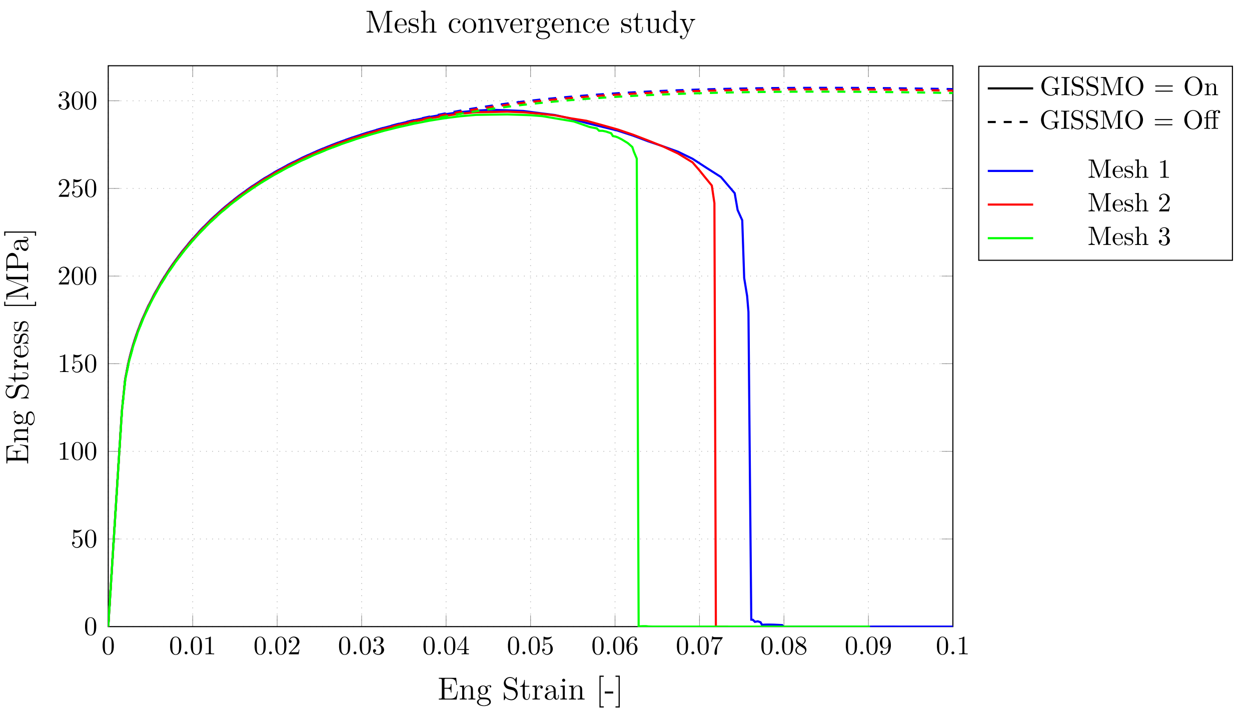

Figure 4.2: Stress strain response for tensile tests of different mesh sizes.

The element size analysis without failure (GISSMO) shows that all tested mesh sizes are sufficiently small and that further refinement does not significantly affect the results. The reason that the failure differs for different element sizes is due to strain localization occurring faster in smaller element, or that the geometry of the pores and particles is not fully resolved. This could give earlier failure strain for finer meshes since mesh regularization for GISSMO is not calibrated for these element sizes. The simulations without GISSMO show a clear convergence for all mesh sizes, which is sufficient to ensure appropriate mesh size with respect to elasto-plastic behavior. In future work, the mesh regularization in GISSMO should be investigated further.

An element length of $0.2\mu m$, resulting in 125 000 elements, is considered sufficient to accurately capture the response while maintaining a reasonable computational cost.

4.3 Conformal versus immersed geometry mesh representation

The microstructural volume elements in this project are built by voxel elements, which is first order hexahedral elements with constant side lengths. In theory, a voxel representation is less capable of capturing complex shapes of silicon and void particles compared to a traditional conformal mesh. The advantage of constructing meshes with voxel elements is that the number of elements remain constant for every generated mesh. It is also complicated to automatically generate conformal (tetrahedral) meshes for volume elements due to limitations of the mesh generator GRFsaw that is used in this work. Figure 4.3 shows two types of solid element.

(a) First order hexahedral element (HEX8).

(b) Second order tetrahedral element (TET10).

Figure 4.3: Two types of solid elements.

However, a mesh element study is conducted in order to evaluate the possibility of capturing the complex geometry of defects with a voxel based mesh compared to a tetra mesh. This is done by modeling a pore which is extracted from a CT-scanned test specimen. The software used for this matter is RETOMO [21], a tool by Beta CAE Systems for 3D-modeling of CT-data. RETOMO has options for producing mesh with both voxel and tetra elements. Figure 4.4 shows an example of a meshed pore extracted from RETOMO, and how the geometry is captured.

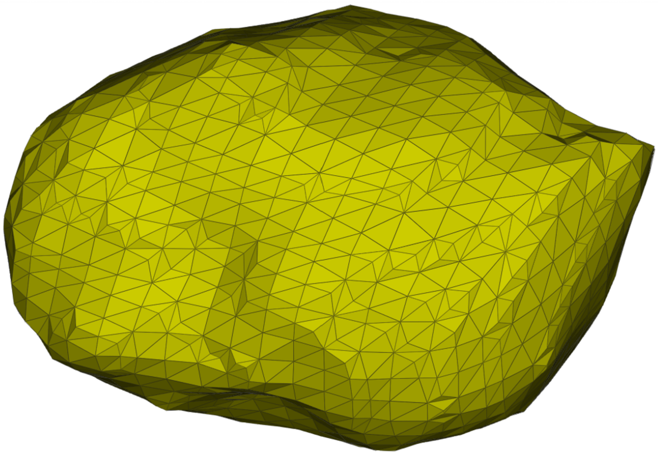

Figure 4.4: Image of CT-scanned pore extracted with RETOMO.

4.3.1 Second-order tetrahedral mesh study of a CT-scanned pore

To analyze how the mesh element size of a second-order tetrahedral mesh influence the accuracy of the results, a mesh study is done. RETOMO is used to export a part of a CT-scanned test specimen that consist of a pore and aluminum, see Figure 4.6. The initial mesh element size is $10\mu m$. In order to refine the mesh, the "Refine tetras"-tool in ANSA is used. This tool divide each tetra element in to eight tetra elements, and is used multiple times to further refine the mesh. The tested mesh sizes is presented in Table 4.2, and the stress-strain response is presented in Figure 4.5

Table 4.2: Number of elements for the tested meshes in Figure 4.5.

Mesh	**No. of elements**
Coarse	94 606
Fine	756 848
Finest	6 054 784

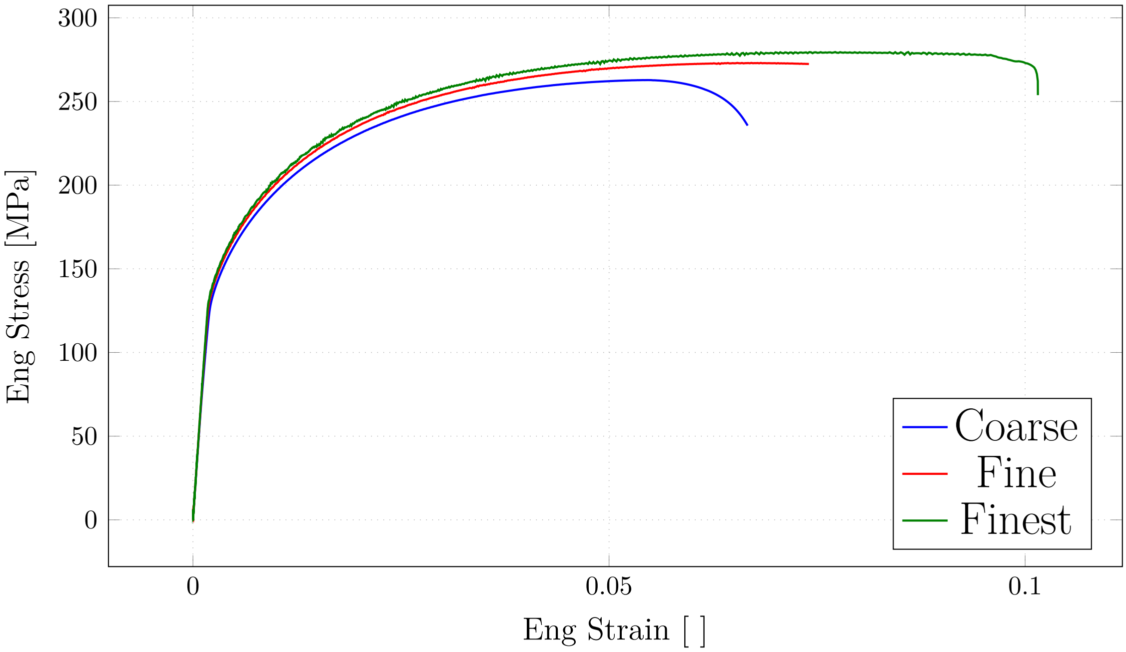

Figure 4.5: Tetra mesh study.

The finest mesh including a pore is shown in Figure 4.6, a cross-section is made through the width and height to illustrate how a pore is meshed with this element size.

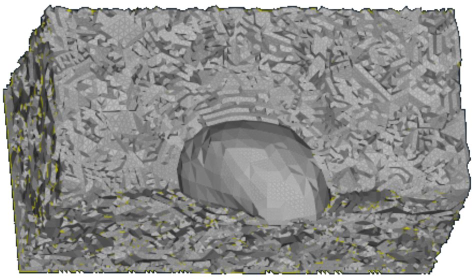

Figure 4.6: Second order tetrahedral "Finest" mesh

4.3.2 First order Hexa mesh study of a CT-scanned pore

When doing the mesh study for the Hexa mesh, the pore is included. This is because the effective properties remain the same, even if the mesh is refined. The tested mesh sizes are presented in Table 4.3. The finer mesh was refined with the Ansa tool "Refine hexas".

Table 4.3: Number of elements for the tested meshes in Figure 4.7.

Mesh	**No. of elements**
Coarse	19 008
Fine	513 216

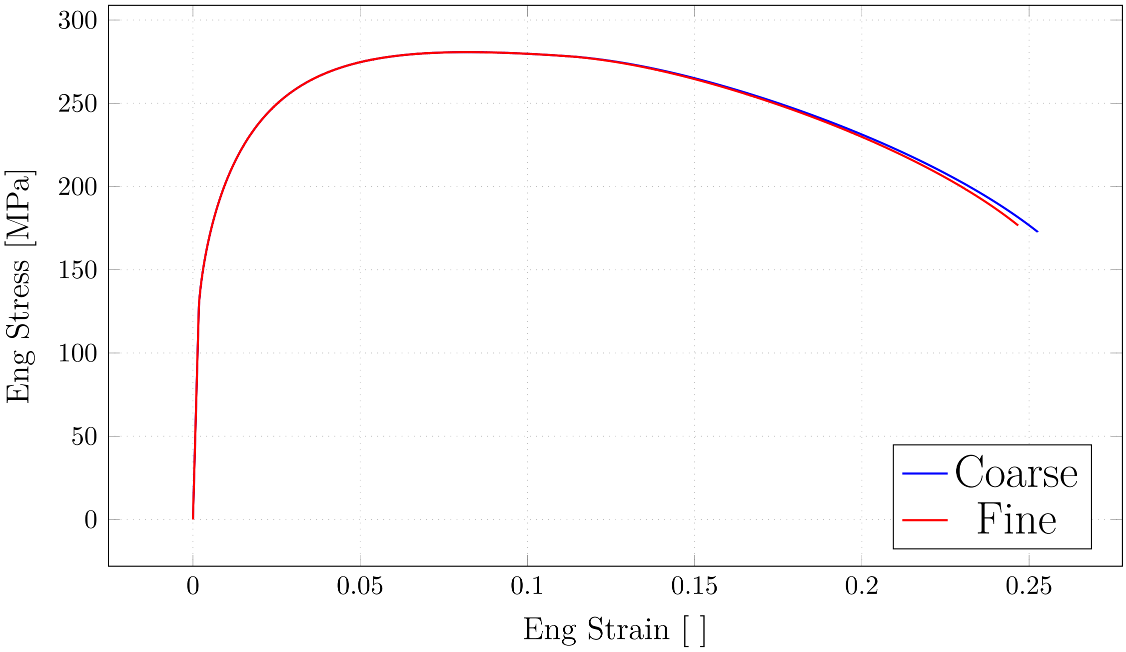

Figure 4.7: Hexahedral mesh quality study.

The mesh convergence study indicates that the solution has converged, demonstrating that the coarse mesh provides sufficient accuracy. Therefore, the standard mesh size exported from RETOMO for hexahedral elements was considered adequate for the simulations.

The mesh for the "Fine" element size is shown in Figure 4.8.

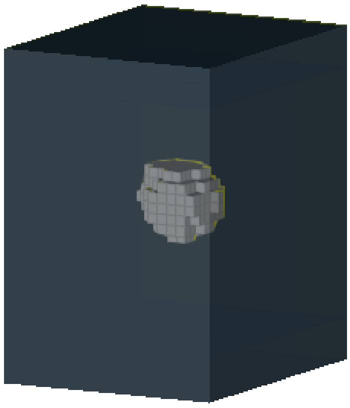

Figure 4.8: First order hexahedral "Coarse" mesh.

4.3.3 Comparison between voxel based and conformal mesh representation of a CT-scanned pore

The finest tetra mesh is being compared to the coarse hexa mesh, with and without pores in Figure 4.9.

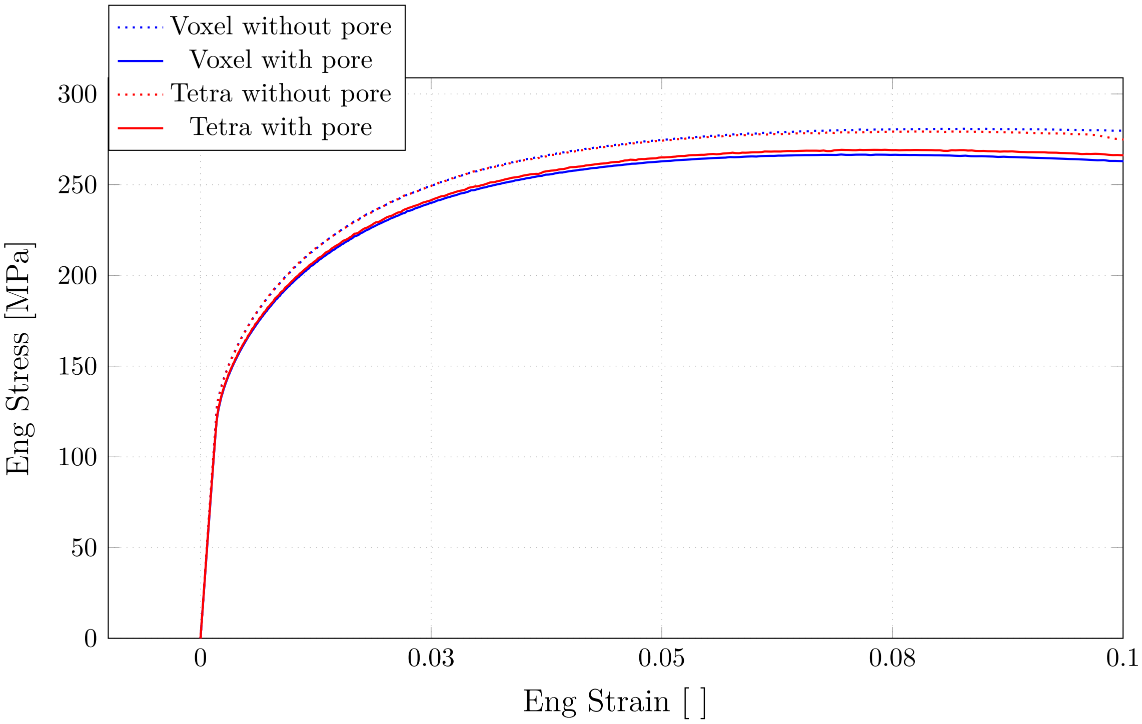

Figure 4.9: Stress-strain for the finest tetra mesh and coarse voxel, with and without a pore. GISSMO is turned off for this study.

The comparison clearly demonstrates that the voxel mesh is equally effective as the tetrahedral mesh in capturing the effects induced by pores, with respect to elasto-plastic properties.

4.4 Size of volume element (RVE study)

If a smaller volume element is extracted from the $10\mu m \times 10\mu m$ mesh, a Statistical Volume Element (SVE) is created. The advantage with an SVE is the reduced computational cost of the simulations. However, the SVE needs to include a sufficient amount of microstructural details to be representative for the whole microstructure in order to obtain accurate results. This is called a Representative Volume Element (RVE), which is commonly used in micromechanical FE-analysis.

Observations from the SEM images showed that the average length of the eutectic area is around $10\mu m$, the microstructure referred to as "Size 2" presented in Table 4.4 is based on that. If a model is smaller then this, it is considered an SVE and if the mechanical behavior of the SVE is the same as for the original model it is considered an RVE.

To study whether an RVE could be used to save computational cost, smaller models are simulated and compared to the "Size 2" model. This model is created with 125 000 elements with 12% Si and 1% porosity. The volume is decreased by deleting one layer of elements on every side to maintain a cubic shape. As the size decrease, the volume fractions also change due to deletion of elements. The tested mesh sizes and corresponding volume fractions are presented in Table 4.4.

Table 4.4: Volume element sizes, contents, dimensions, and volume reduction.

Size	**Side length** (μm)	**No. of elements**	**Volume reduction (%)**	**Silicon (%)**	**Porosity (%)**
Size 1	12.5	244 140	0.0	12	1
Size 2	10	125 000	48.8	11.9	1
Size 3	7.5	53 734	78.4	11.6	1
Size 4	5	15 625	93.6	10.6	0.6
Size 5	2.5	1 954	99.2	11.1	1.4

Periodic boundary conditions are applied to the models with prescribed macroscopic displacement gradient $\mathbf{H}_{22} = 0.1$ to simulate a uniaxial tensile test. The mechanical response is compared in order to evaluate if the SVE is representative or not.

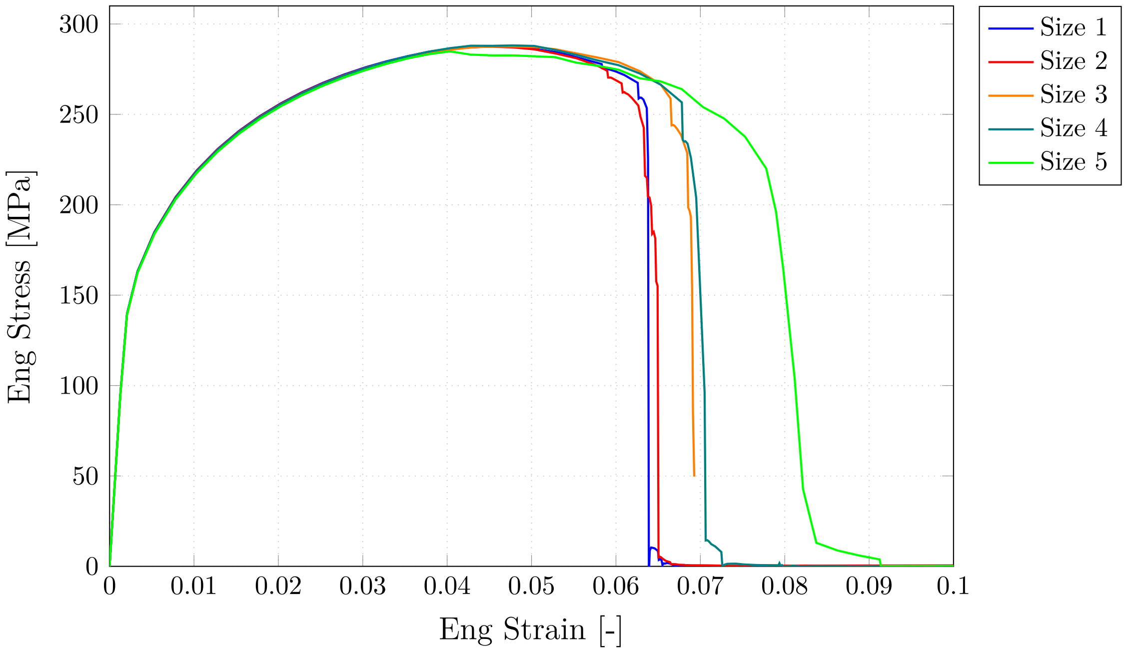

Figure 4.10: RVE study, tensile tests with periodic boundary conditions.

One of the main observations for this material is the variation of mechanical behavior caused by the stochastic morphology and defects in the microstructure. The results in Section 5 shows that the "Size 2" model has a variation in the mechanical behavior only from changing the location of different phases, even if the same volume fraction of silicon and particles is used. This variation is almost as significant as in the study done here for different sized volume elements. Therefore, it is difficult to determine if the variation of the mechanical behavior in this study is due to the volume element being too small or if this is the variation that could be observed even if the size remained constant.

The size of the model, Size 2, could be considered representative since it can be observed in the SEM images of the eutectic and is therefore the size that is being used for the following studies.

If an RVE study should be done correctly, a sufficient amount of varying microstructure needs to be simulated in order to establish the deviation of the mechanical behavior. This deviation can then be used as a criteria for the SVE in order to be considered representative.

4.5 Implicit vs Explicit time integration with LS-DYNA

For transient FE-analysis, time is taken in to consideration. Just as the model is divided in to finite elements in all dimensions, the time can be seen as the fourth dimension. This means that the time also have to be discretized. In order to solve the equation of motion in the time domain, the time is divided in to a finite number of time steps expressed as:

$$\Delta t = t_{n+1} - t_n \tag{4.1}$$

This is known as the time integration method, where the unknown values are calculated based on their previous known values:

$$u(t_{n+1}) = u(t_n) + \Delta t \dot{u} \tag{4.2}$$

$$\dot{u}(t_{n+1}) = \dot{u}(t_n) + \Delta t \ddot{u} \tag{4.3}$$

where the value for t_{n+1} is determined by the derivative of the function.

4.5.1 Explicit and Implicit time integration

The time integration is divided in two different methods, explicit and implicit time integration. Explicit time integration uses the slope at the known time step to determine the unknown. Using Equation 4.2 as reference, the explicit time integration is:

$$u(t_{n+1}) = u(t_n) + \Delta t \dot{u}(t_n) \tag{4.4}$$

Since the values on the R.H.S are known, the unknown values are directly calculated and the accuracy is determined by the size of the time step Δt. The time step is determined by the smallest element length L_{min} and the longitudinal dilation wave speed $c_d = \sqrt{E/\rho}$, where E is Young's modulus and ρ is the density of the material:

$$\Delta t \leq \frac{L_{min}}{c_d} \tag{4.5}$$

The criterion prevent the dilation wave to travel further than the smallest element length in a time step. In FE-models with small elements, this criterion can result in a very small time step which leads to computationally expensive simulations. In order to increase the time step, the density of the material can be increased artificially which increases the value of c_d. This is called mass scaling, and it should not be overdone since it impacts the results.

The implicit method on the other hand, calculates the derivative of the unknown time step in order to solve the equation:

$$u(t_{n+1}) = u(t_n) + \Delta t \dot{u}(t_{n+1}) \tag{4.6}$$

Since there are two unknown variables, a set of non-linear equations have to be solved using numerical methods. This is computationally expensive, but gives a stable solution no matter the time step. However, the implicit solution still gets inaccurate if the time step is too large [22], [23].

With LS-DYNA R16, the version used in this project, simulations with PBC using *RVE_ANALYSIS_FEM is only possible with implicit time integration. However, an experimental version is investigating the implementation of PBC with explicit time integration. This version is investigated in this project to explore the possibilities with explicit FEM. The possible advantage of simulating PBC with explicit time integration is that the computations can be spread out over many cores more efficiently to increase the total computational speed. The pre-processing of the explicit setup with PBC is more complicated and time consuming for this case.

4.5.2 Results - Implicit vs Explicit

To compare the results and computational time for explicit vs implicit with periodic boundary conditions two models are used. The smaller mesh has 19008 elements with a pore volume fraction of 1.5%. The bigger model has 125000 elements, the pore volume fraction is 1% and the silicon volume fraction is 12%. Both the implicit and explicit models uses PBC with tensile loading.

Earlier, in Section 3.4, it was mentioned that the keyword *RVE_ANALYSES_FEM, that applies PBC, only is compatible with an implicit solver. In order to use PBC with an explicit solver, a keyword called *INCLUDE_UNITCELL is used. During this project, this method was still under development by LS-DYNA and the information about the implementation is therefore limited. However, similarly to *RVE_ANALYSIS_FEM, the keyword automatically applied PBC to the model.

For the implicit simulations, both the big and small microstructures are solved with 120 cores. Increasing the amount of cores did not improve the simulation time. For the explicit simulation, the smaller model microstructure uses 120 cores while the larger microstructure model uses 256 cores. The mechanical response of the simulations are presented in Figure 4.11 as stress-strain curves from virtual tensile tests. The simulation times for the experiments are presented in Table 4.5.

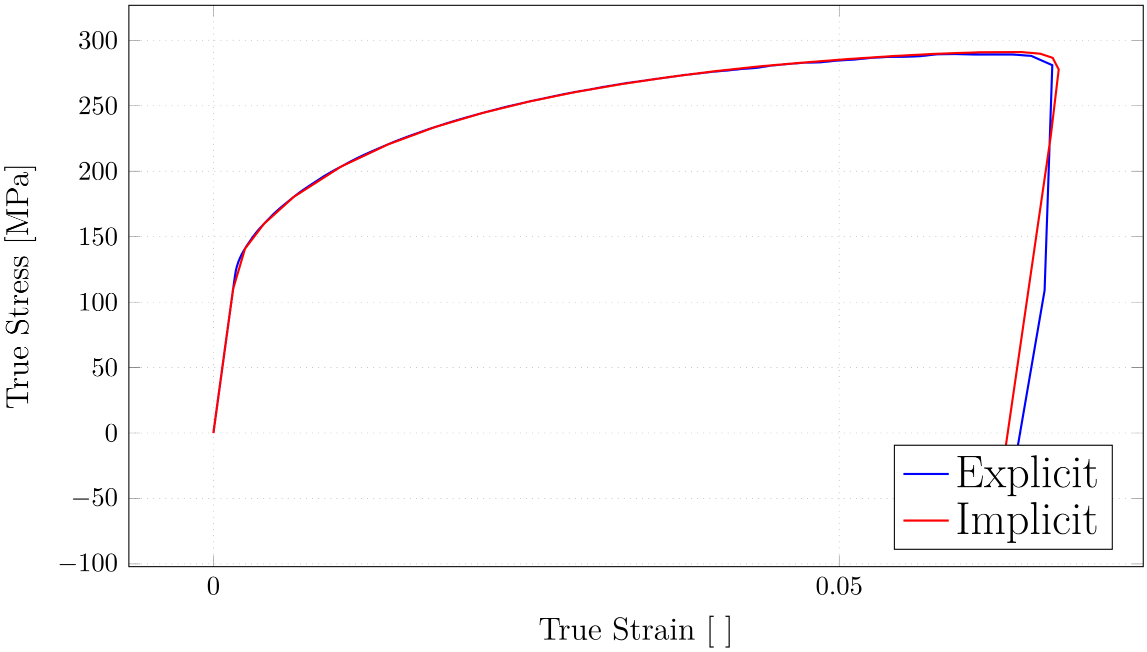

Figure 4.11: Explicit vs Implicit simulations with PBC

The explicit and implicit simulations with PBC gives a similar mechanical response.

Table 4.5: Simulation time for implicit and explicit with PBC.

Simulation	N = 19 008	N = 125 000
Explicit	40 min & 0 sec	9 hour & 7 min
Implicit	4 min & 3 sec	1 hour & 46 min

To further reduce the simulation time, a termination sensor is added to the model. This will terminate the simulation if a defined time and stress are fulfilled. In this model, the simulation ends if the time is greater then half the simulation time and the stress is lower than 260 MPa. This is right after the failure for these simulations, and the termination sensor prevent unnecessary computations after this point. The simulation time for this is shown in Table. 4.6.

Table 4.6: Simulation time for implicit and explicit with PBC.

Simulation	N = 19 008	N = 125 000
Explicit	28 min & 47 sec	N/A
Implicit	1 min & 34 sec	11 min & 58 sec

The implicit solver has a much lower simulation time and is therefore used with PBC in this project.

5

Influence of eutectic morphology and defects on mechanical response

Two variations of morphology and defects are studied in the following section. The first study analyzes how the different volume fraction of silicon is changing the mechanical behavior of the material. In the second study we investigate the volume fraction of silicon while pores are kept constant but the placement of the phases is allowed to change location in the microstructure.

5.1 Mechanical response

In order to analyze how the variation of defects impact the mechanical properties such as stiffness, strength and ductility, stress-strain curves from simulations are presented to visualize this.

5.1.1 Variation of silicon and porosity volume fractions

The eutectic regions of HPDC aluminum components possess a variation in volume fraction of silicon and porosity depending on the distance from the cast inlet, also through the thickness. By enabling the GRF-saw script in Section 2.3 to alter the volume fraction of the different phases, homogenization of the material properties could be done, either for the whole component or sections of the component.

Five samples are simulated with varying volume fraction of silicon to analyze the effect of this phase. The volume fraction of silicon varies from 7% to 15%.

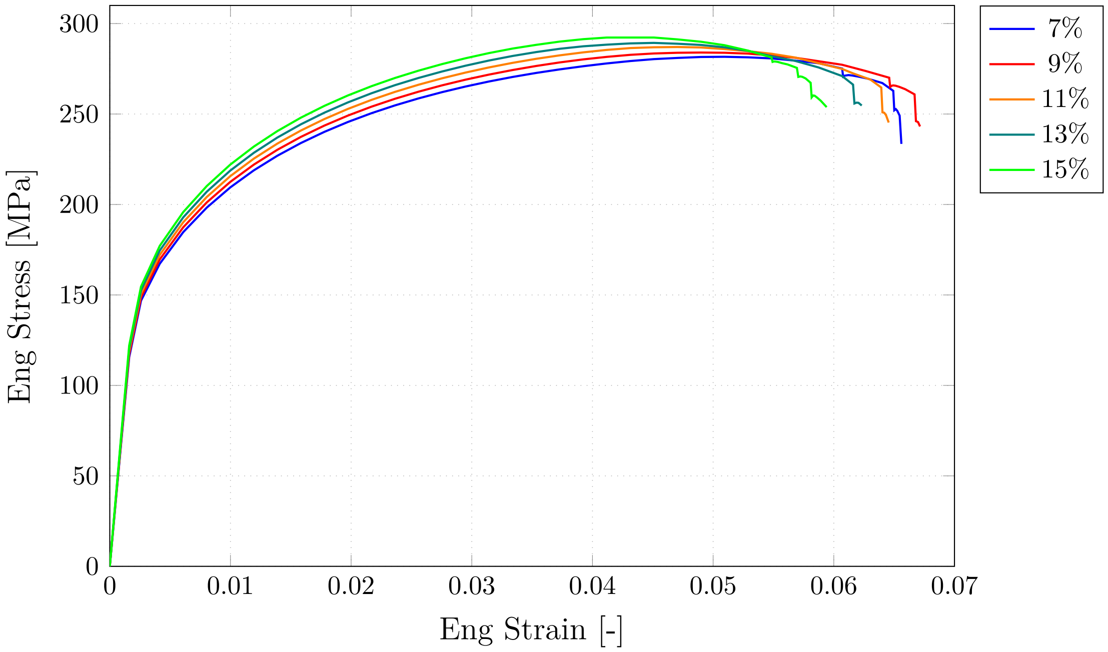

Figure 5.1: Stress-strain response for 5 simulations with varying silicon content.

An increase in silicon content clearly leads to a stiffer material, as indicated by the higher Young's modulus. At the same time, the material becomes stronger, which is reflected in the increased maximum stress. However, this improvement in stiffness and strength is accompanied by a reduction in ductility, as evidenced by the lower failure strain.

5.1.2 Placement of silicon particles and pores

To examine how the microstructural morphology impacts the mechanical properties, 10 microstructures are generated. The input settings such as volume fractions and target particle size are kept constant for all volume elements, and the seeds are swept in order to alter the placement of the particles. Figure 5.2 presents the complete stress-strain curves for the simulated microstructures. Figure 5.3 shows the same results but zoomed in on the failure region in order to visualize the variation in detail. All microstructures are loaded as in tensile tests.

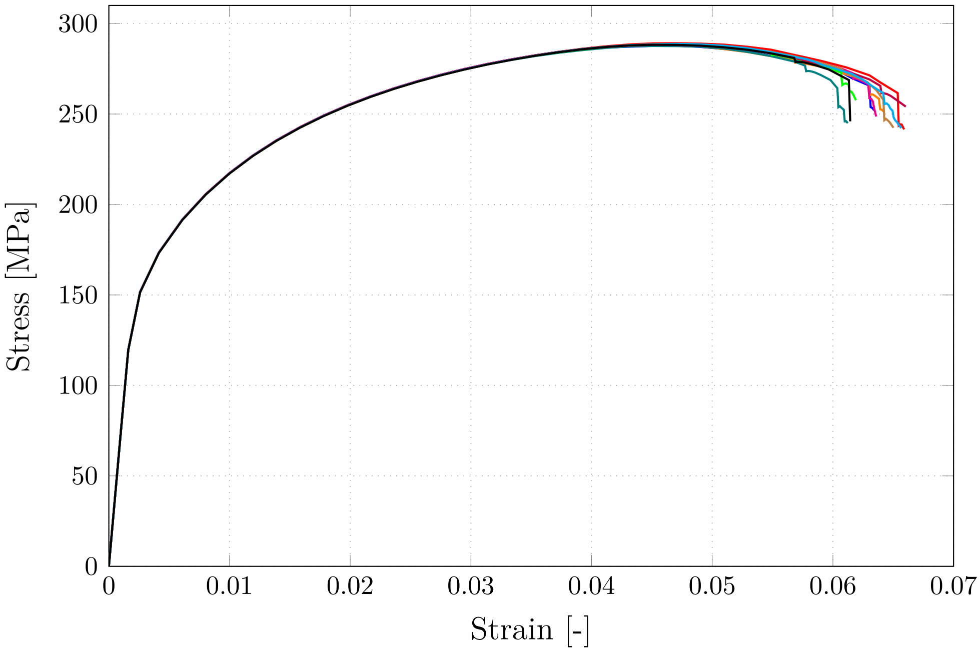

Figure 5.2: Stress-strain response for 10 unique volume elements with identical prescribed microstructural properties.

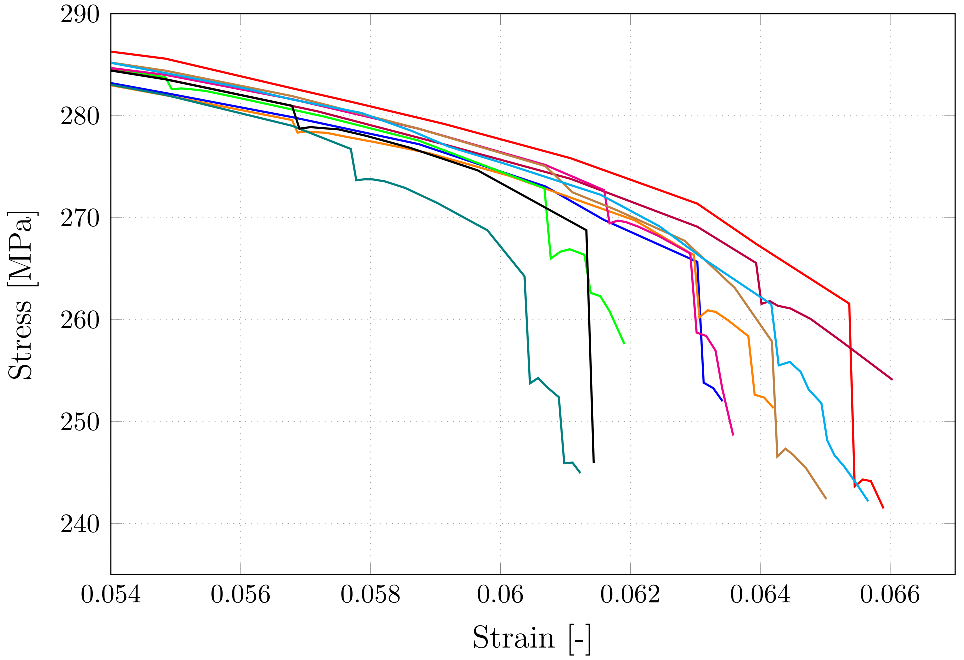

Figure 5.3: Detailed view showing plastic failure strain of Figure 5.2.

The spread of failure strain is roughly ±5% in Figure 5.3. Since the volume fractions are identical for all the microstructures, the variation is purely due to the placement and size of the particles. Morphological properties such as particle sizes and internal distribution result in varying crack propagation when comparing the different simulations. Figure 5.4 and 5.5 present the plastic strain distribution on the surface of the volume element with the lowest and highest failure strain. Both scalar plots are extracted at the same homogenized tensile strain level during the experiments, $\varepsilon_{yy} = 0.061$. The reason for this is to visualize how the plastic strain distribution depend on particle distribution. Visual deformation is deactivated in the scalar plots.

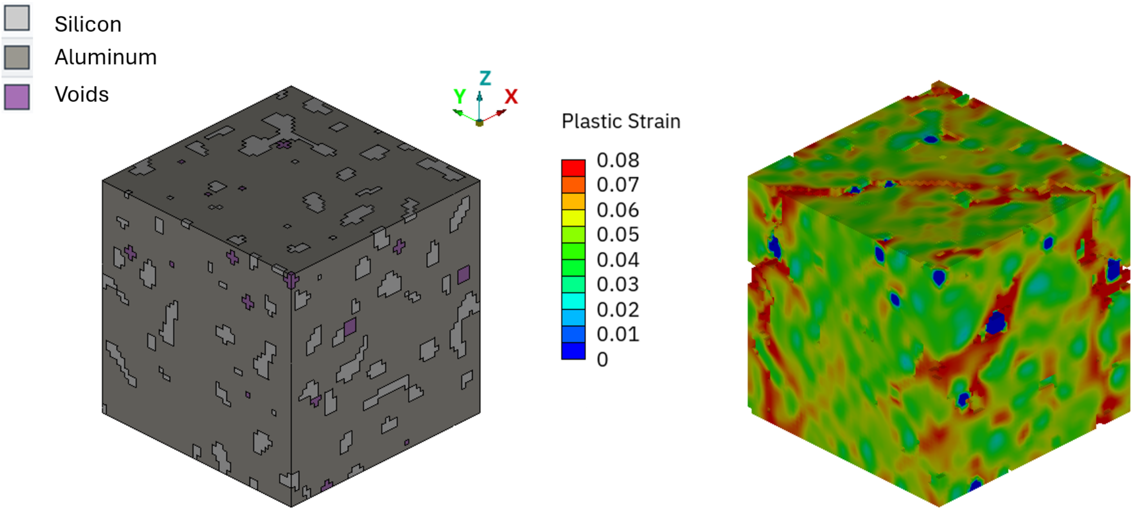

Figure 5.4: Microstructural phases (left) and plastic strain (right) at $\varepsilon_{yy} = 0.061$ on surface of the volume element with the lowest tensile fracture strain.

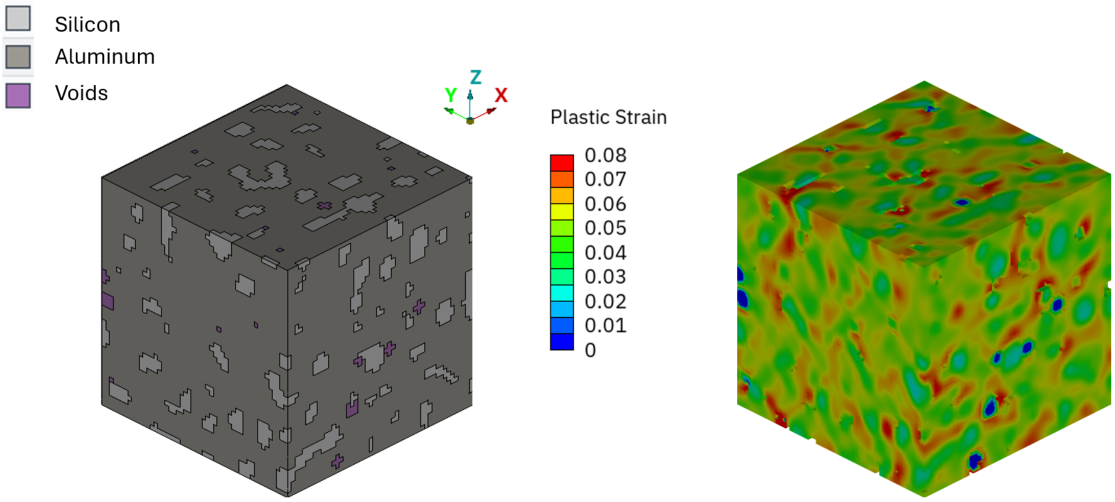

Figure 5.5: Microstructural phases (left) and plastic strain (right) at $\varepsilon_{yy} = 0.061$ on surface of the volume element with the highest tensile fracture strain.

In Figure 5.4, a higher level of porosity can be observed near the surface, with pores located in close proximity to each other. This clustering facilitates strain localization and crack propagation between neighboring pores. In contrast, the model shown in Figure 5.5 contains fewer pores at the surface, and these are more evenly distributed throughout the material. As a result, stress concentrations are less pronounced, making strain localization and crack initiation less likely.

5.1.3 Anisotropy

In order to see how the loading direction impacts the mechanical properties, tensile tests in x-, y-, and z-direction are compared. The simulations are performed on the same microstructure with 12% silicon and 1% porosity. The stress-strain responses are presented in Figure 5.6.

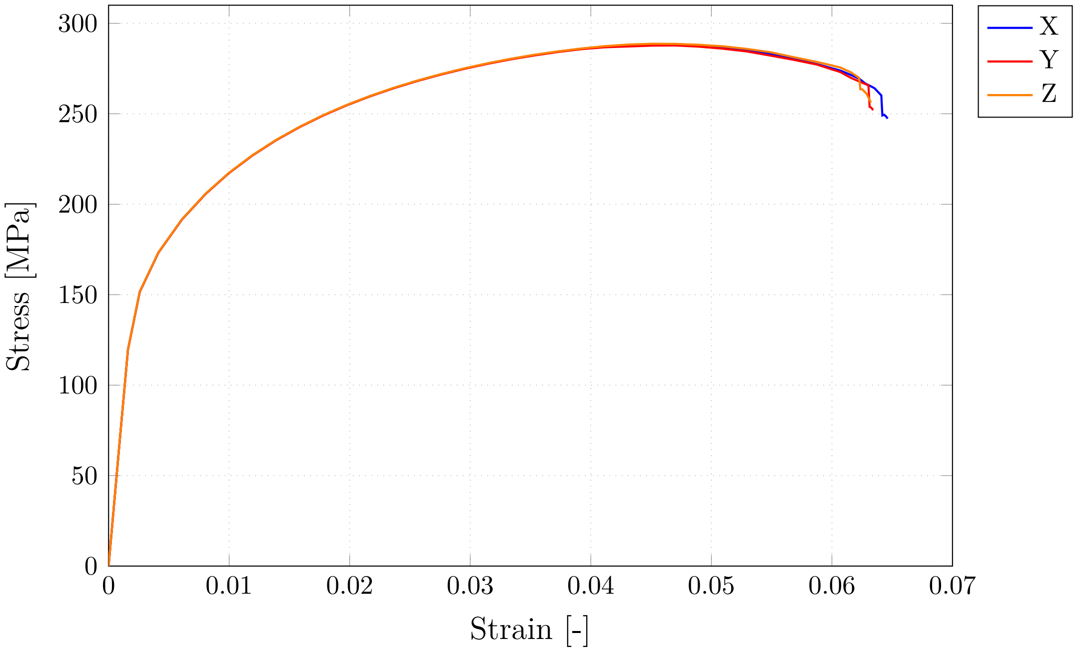

Figure 5.6: Stress-strain response for different tensile load directions for the same microstructure.

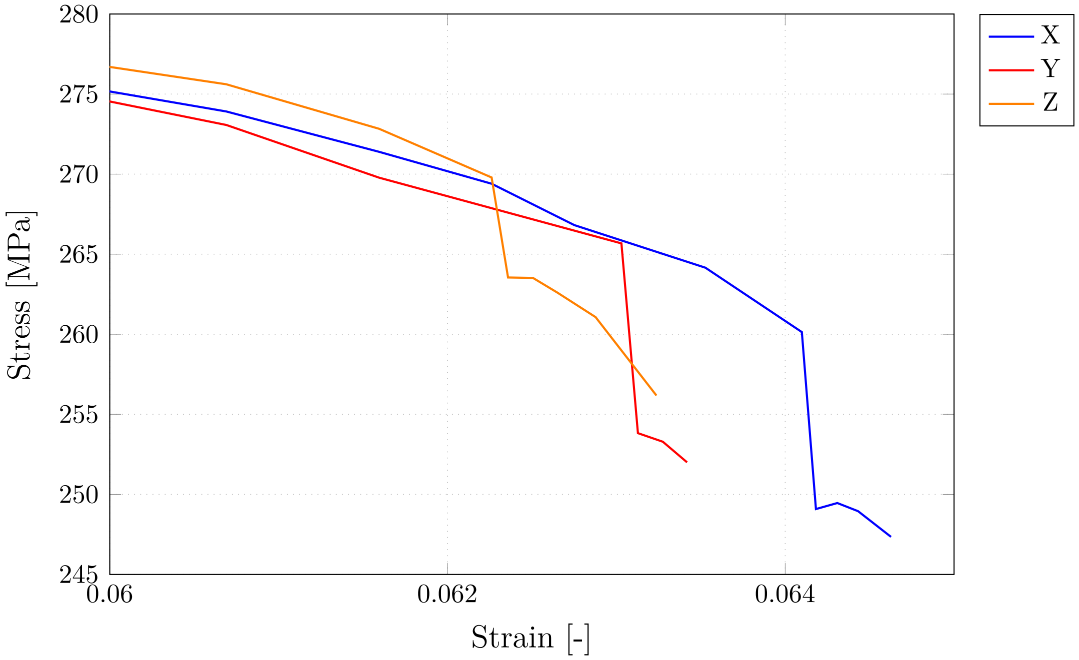

Figure 5.7: Failure strain from Figure 5.6.

The response shows that the failure behaves differently depending on what loading direction is applied. However, only small differences can be observed. This concludes that mechanical data from three tensile tests can be extracted from a single volume element. The study of anisotropy in this project is only performed on tensile tests. However, there is nothing in the modeling that is anisotropic. Hence the directional variation is a sign of small randomness.

5.2 Failure strain vs triaxiality

In this Section, the failure strain vs triaxiality for different studies are presented. This is done to clearly show how the failure of different load cases, depend on placement of phases and different volume fractions. The plastic failure strain vs triaxiality curve is also an important homogenized property for failure in the material. For 3D solid elements with GISSMO damage model, a Lode parameter dependency is also present. However, for presentation purposes, the Lode parameter dependency is not presented in the following results.

5.2.1 Load cases

A specimen with 12% silicon and 1% porosity was simulated for tensile, shear, biaxial, lateral and compression and the results are shown in Figure 3.6. From these simulations, the triaxiality and failure plastic strain were calculated and extracted.

In Figure 5.8 two splines are created from the same simulation used in Figure 3.6. The solid spline is created from the failure plastic strain value for compression, shear, tensile, laterally confined tensile and biaxial simulations. The dashed spline is created from the same failure plastic strain, but four extra load cases are added. These extra load cases are compression+shear, two variations of tensile+shear and laterally confined tensile+biaxial.

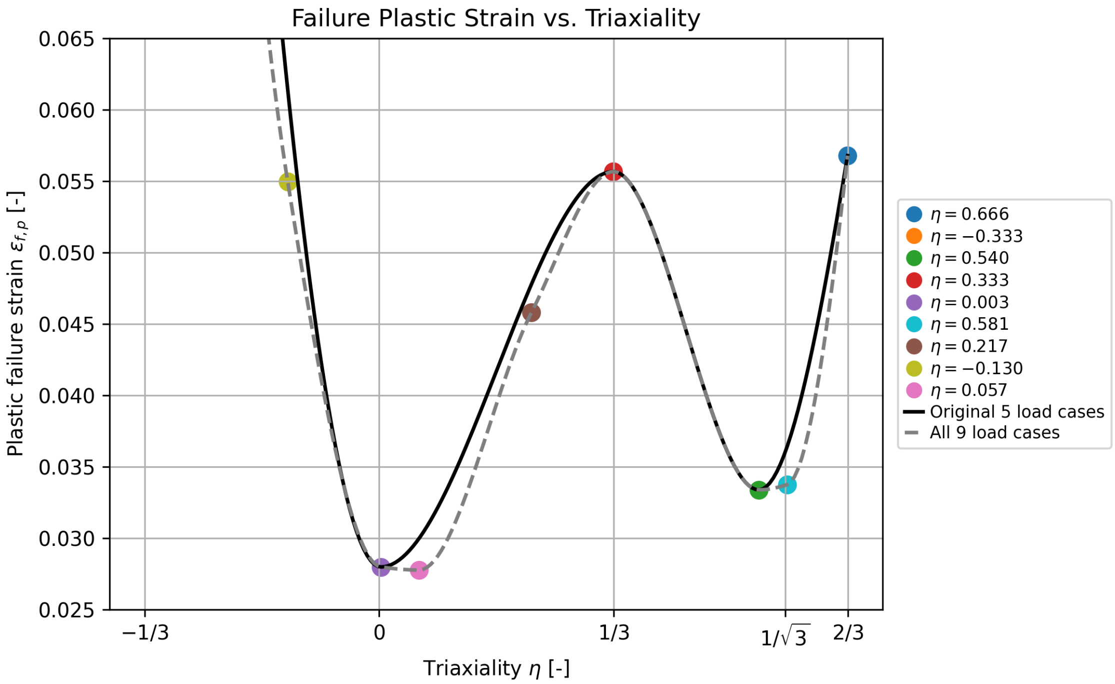

Figure 5.8: Failure plastic strain vs Triaxiality with extra load cases.

Between $\eta = 0$ and $\eta = 1/3$, two of the extra load cases were added, the new spline took a more linear shape compared to the original spline. However, the new load case at $\eta = 0.581$ created a less linear spline. Since the spline is too linear at one point, but not curved enough at another, the approximation of the failure plastic strain is improved by adding extra load cases.

5.2.2 Influence of phases

In Figure 5.9 three different curves are displayed. The curve at the top, labeled **"Al"**, is 100% aluminum. Under that curve is aluminum with 1% porosity, labeled **"Al+Pores"**. The last curve at the bottom, labeled **"Al+Si+Pores"**, is aluminum with 1% porosity and 12% silicon. This is the same microstructure as in Figure 5.8 with the original load cases.

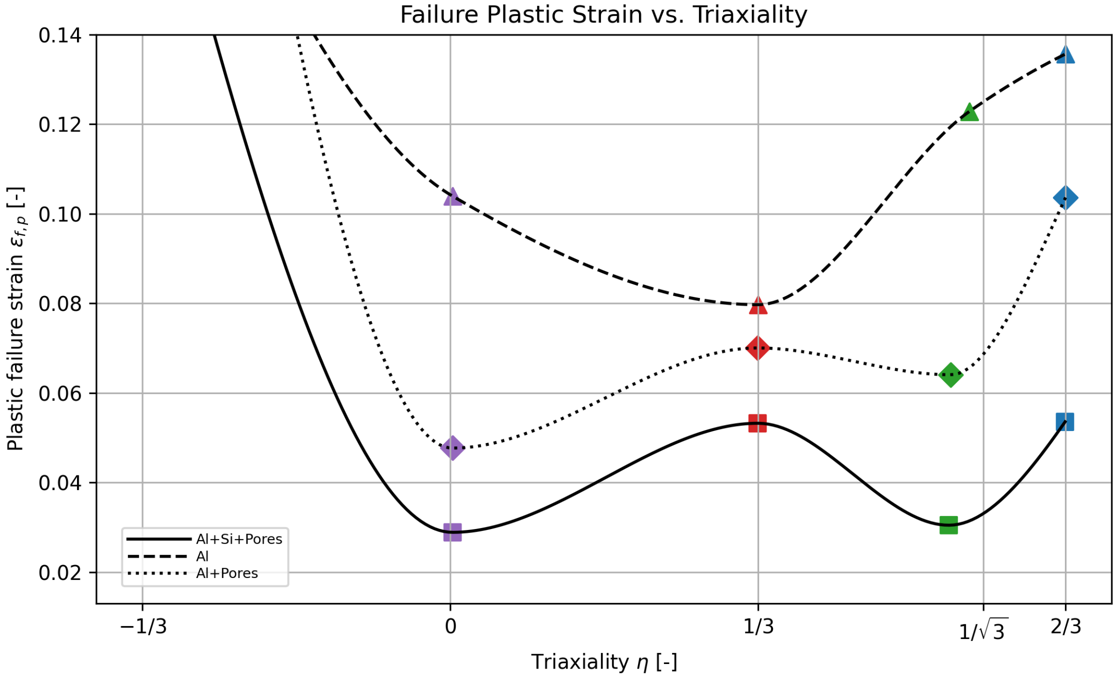

Figure 5.9: Failure plastic strain vs Triaxiality for microstructures with different contents.

Similar to the results in Figure 5.2, the material gets less ductile when silicon is added and therefor results in a lower failure strain.

A notable observation from these results is that the addition of porosity and silicon particles does not lead to a linear reduction in plastic failure strain across the different load cases. Instead, the relative behavior between the load cases changes.

For pure aluminum, the highest failure strain is observed under biaxial loading, followed by lateral loading, shear, and finally tensile loading. When porosity is introduced, the failure strain in biaxial, lateral, and shear loading decreases more than in tensile loading. As a result, tensile loading exhibits a higher failure strain than both lateral and shear cases.

Finally, with the addition of silicon, the difference between tensile and biaxial loading diminishes, and both load cases exhibit approximately the same failure strain.

5.2.3 Influence of morphology

In Figure 5.10 below two samples are shown. **Sample 1** and **Sample 2** have the same volume fraction, 12% silicon and 1% pores, but the phases are randomly distributed in the model.

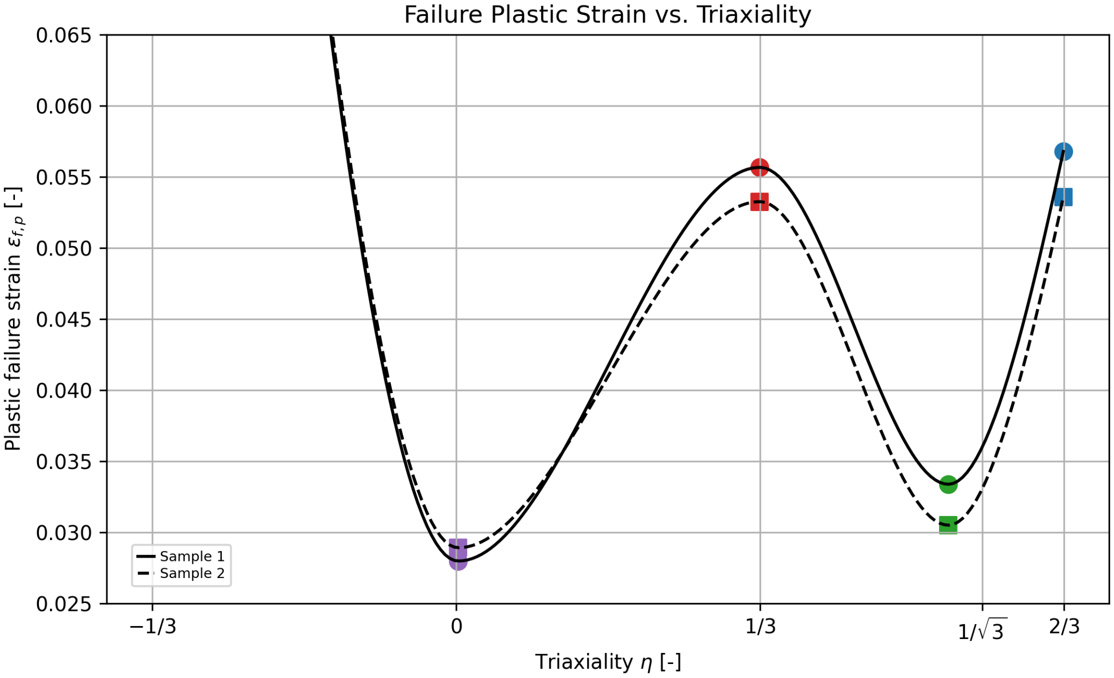

Figure 5.10: Failure plastic strain vs Triaxiality for different microstructures.

This study clearly shows the complexity of the material behavior. `Sample 1` has a higher plastic failure strain when simulated with biaxial, laterally confined tensile and tensile loading compared to `Sample 2`. But for shear, `Sample 2` experiences a higher plastic failure strain.

This further argues for the benefits of adding more load cases, like in 5.8, to get a better approximation for the modeling of failure. In addition, for lower triaxiality the difference between the samples seems smaller.

6

Conclusion and future work

This Chapter presents the conclusions drawn from the results based on the objectives of the project, as well as proposals for future work on the topic.

6.1 Conclusion

The objective of this thesis was to develop a method that creates representative microstructure models in order to analyze how variations in defects within the microstructure of HPDC aluminum influence its mechanical behavior, while taking into account the effects of different FE mesh strategies, mesh resolutions, boundary conditions, and time integration techniques with respect to accuracy and computational cost.

To investigate this, a method for generating virtual microstructures was developed, enabling the study of how defects affect mechanical behavior. In order to validate this approach, several key aspects were established:

- Periodic boundary conditions (PBC) were found to be more appropriate than linear displacement boundary conditions (LDBC).
- An element size of $0.2\,\mu m$ for meshing silicon particles of approximately $1\,\mu m$, in combination with hexahedral elements, was shown to provide a sufficient representation of the microstructure, with respect to elasto-plastic properties. Furthermore, the GRFsaw script was demonstrated to generate representative meshes.
- No definitive conclusions regarding the representativeness of the RVEs can be drawn without a more extensive study of the statistical variation in the full-scale model.
- Increasing the number of applied load cases improves the accuracy of the resulting triaxiality curve.
- Implicit solvers were found to be better suited for this type of analysis, particularly when using PBC in LS-DYNA.
- Hexahedral elements were shown to be a viable alternative to tetrahedral elements.

The GRF-saw script has demonstrated the capability to generate microstructures that are representative both visually and in terms of mechanical response. Compared to CT-based approaches, this method provides a faster and more flexible alternative, as key microstructural features such as volume fraction, particle size, and shape can be systematically controlled and varied. CT-scan has also the limitation that not all relevant microstructural components (such as Si particles) can be detected.

The presented method, together with the analyzed results, provides a solid foundation for future work on the homogenization of the eutectic region and the development of multiscale models for HPDC aluminum.

6.2 Future work

Future work that expand upon this project are presented in this section.

- A similar method can be used to model beyond the eutectic region in order to simulate a larger scale that include the eutectic region, the intermetallics and the α-aluminum phase.
- This project does not implement slip conditions to account for delamination between the different phases, this can be implemented and analyzed further.
- Other numerical methods, for example Fast Fourier Transform (FFT), can be investigated and compared to FEM. Explicit FE-simulations with PBC can be investigated more in detail. This could increase computational efficiency, which is beneficial if simulations are to be made on a larger scale.
- More simulations need to be done in order to do a RVE size study. It is debatable if the RVE study in this project is sufficient enough to draw conclusions regarding representativeness.
- The chosen fracture modeling show mesh dependent results whereby mesh regularization for GISSMO could be studied further.
- In this project, information about morphology is acquired by studying 2D SEM images in order to construct representative 3D models. Improvements on the microstructure model generation can be implemented so that 2D SEM images can be directly used as input data for 3D generations.

Bibliography

[1] Budenheim, *How to boost e-mobility efficiency?* `https://www.budenheim.com/polymers/knowledge-base/e-mobility-efficiency`, Accessed: 2026-01-23, 2026.

[2] M. Merchán et al., "High-pressure die casting (hpdc) process parameters optimization for al-mg-fe aluminum alloy structural parts manufacturing," *Metals*, vol. 15, no. 10, 2025, ISSN: 2075-4701. DOI: `10.3390/met15101071`. [Online]. Available: `https://www.mdpi.com/2075-4701/15/10/1071`.

[3] P. Burggräf, G. Bergweiler, S. Kehrer, T. Krawczyk, and F. Fiedler, "Megacasting in the automotive production system: Expert interview-based impact analysis of large-format aluminium high-pressure die-casting (hpdc) on the vehicle production," *Journal of Manufacturing Processes*, vol. 124, pp. 918–935, 2024, ISSN: 1526-6125. DOI: `https://doi.org/10.1016/j.jmapro.2024.06.028`. [Online]. Available: `https://www.sciencedirect.com/science/article/pii/S152661252400608X`.

[4] Volvo Cars, *Megacasting, Volvo Cars Torslanda*, `https://www.volvocars.com/se/l/torslanda/megacasting/`, Accessed: 2026-02-20, 2026.

[5] M. Murray and M. Murray, "9 - high pressure die casting of aluminium and its alloys," in *Fundamentals of Aluminium Metallurgy*, ser. Woodhead Publishing Series in Metals and Surface Engineering, R. Lumley, Ed., Woodhead Publishing, 2011, pp. 217–261, ISBN: 978-1-84569-654-2. DOI: `https://doi.org/10.1533/9780857090256.1.217`. [Online]. Available: `https://www.sciencedirect.com/science/article/pii/B9781845696542500092`.

[6] Science Insights, *How microstructures control material properties*, `https://scienceinsights.org/how-microstructures-control-material-properties/`, Accessed: 2026-05-25, Nov. 2025.

[7] Mechanics of Materials Lab, University of Oxford, *Multi-scale material modelling*, `https://mechmat.web.ox.ac.uk/multi-scale-material-modelling`, Accessed: 2026-05-25, n.d.

[8] W. Abel and V. Kullberg, "Virtual material characterization of natural fibre composites," Bachelor's thesis, Department of Industrial and Materials Science, Gothenburg, Sweden, 2024.

[9] Total Materia. "Aluminum-silicon alloys," Total Materia, Accessed: May 11, 2026. [Online]. Available: `https://www.totalmateria.com/en-us/articles/aluminum-silicon-alloys/`.

[10] F. Niklas. "The aluminum-silicon alloy connection," Casting-Campus GmbH, Accessed: May 11, 2026. [Online]. Available: `https://casting-campus.com/the-aluminum-silicon-alloy-connection/`.

[11] S. Hegde and K. N. Prabhu, "Modification of eutectic silicon in al–si alloys," *Journal of Materials Science*, vol. 43, no. 9, pp. 3009–3027, 2008, ISSN: 1573-4803. DOI: `10.1007/s10853-008-2505-5`. [Online]. Available: `https://doi.org/10.1007/s10853-008-2505-5`.

[12] L. Blatny, *Grfsaw: A lightweight stochastic microstructure generator*, `https://github.com/larsblatny/GRFsaw`, Accessed: 2026-03-31, 2024.

[13] L. Blatny, H. Löwe, and J. Gaume, *Grfsaw: A lightweight stochastic microstructure generator*, 2024. arXiv: `2412.05168 [cs.CE]`. [Online]. Available: `https://arxiv.org/abs/2412.05168`.

[14] L. Blatny, H. Löwe, S. Wang, and J. Gaume, "Computational micromechanics of porous brittle solids," *Computers and Geotechnics*, vol. 140, p. 104 284, 2021, ISSN: 0266-352X. DOI: `https://doi.org/10.1016/j.compgeo.2021.104284`. [Online]. Available: `https://www.sciencedirect.com/science/article/pii/S0266352X21002822`.

[15] ANSYS, Inc., *LS-DYNA Keyword User's Manual*, Release 16, ANSYS, Inc., Canonsburg, PA, USA, 2023. Accessed: May 4, 2026. [Online]. Available: `https://lsdyna.ansys.com/wp-content/uploads/2025/04/LS-DYNA_Manual_Vol_II_R16.pdf`.

[16] A. Haufe, P. DuBois, F. Neukamm, and M. Feucht, "Gissmo – material modeling with a sophisticated failure criteria," in *LS-DYNA Developer Forum*, DYNAmore GmbH, Stuttgart, Germany, 2011. [Online]. Available: `http://www.dynamore.de`.

[17] Fidelis Engineering Associates. "What is stress triaxiality? and why does it matter in ductile damage modeling?" Accessed 7 May 2026. [Online]. Available: `https://www.fidelisfea.com/post/what-is-stress-triaxiality-and-why-does-it-matter-in-ductile-damage-modeling`.

[18] EWI. "New damage model to improve metal failure prediction." Accessed 7 May 2026. [Online]. Available: `https://ewi.org/new-damage-model-to-improve-metal-failure-prediction/`.

[19] COMSOL AB, *Homogenization of material properties*, Accessed: 2026-05-18, n.d. [Online]. Available: `https://www.comsol.com/support/learning-center/article/homogenization-of-material-properties-80311`.

[20] ANSYS, Inc., *LS-DYNA Keyword User's Manual*, Release 16, ANSYS, Inc., Canonsburg, PA, USA, 2023. Accessed: May 4, 2026. [Online]. Available: `https://lsdyna.ansys.com/wp-content/uploads/2025/04/LS-DYNA_Manual_Vol_I_R16.pdf`.

[21] BETA CAE Systems, *RETOMO: The key to 3D-modeling from CT-data of physical objects*, `https://www.beta-cae.com/retomo.htm`, Accessed: 2026-05-22, n.d.

[22] Fidelis Engineering Associates, *Time integration methods for implicit and explicit fea: What are they and how do they work?* `https://www.fidelisfea.com/post/time-integration-methods-for-implicit-and-explicit-fea-what-are-they-and-how-do-they-work`, Accessed: 2026-04-08, 2022.

[23] ANSYS, Inc., *Lesson 2: Implicit and explicit time integration*, `https://innovationspace.ansys.com/courses/wp-content/uploads/sites/5/`

`2021/02/Lesson2_ImplicitAndExplicitTimeIntegration-1.pdf`, ANSYS Innovation Space course material, accessed: 2026-04-08, 2021.

DEPARTMENT OF SOME SUBJECT OR TECHNOLOGY
CHALMERS UNIVERSITY OF TECHNOLOGY
Gothenburg, Sweden
www.chalmers.se

CHALMERS
UNIVERSITY OF TECHNOLOGY